8-1-2017

Measuring and Modeling the Conductivity of Highly Insulating Materials

David King
Utah State University

Measuring and Modeling the Conductivity of Highly Insulating Materials

David King

Department of Physics
4900 Project
Research Mentors: Brian Wood and J.R. Dennison
August 1, 2017

I. INTRODUCTION

Satellites and other spacecraft must be able to withstand hazardous conditions in order to be viable in their expected operating environments. One specific hazard that occurs due to incident radiation is spacecraft charging. Insulating materials, frequently used in spacecraft and other electrical equipment, while very good at preventing charge flow, also store charge very well. This can create problems; specifically, "if the charge decay time exceeds the orbital period, not all charge will be dissipated before orbital conditions act again to further charge the satellite. As the insulator accumulates charge, the electric field will rise until the insulator breaks down" [1]. Thus, understanding the mechanisms that dictate conductivity, or how charge flows, in insulating materials is of critical importance for determining spacecraft charging effects with these materials.

Materials of particular interest in this study are highly disordered insulating materials (HDIM), specifically highly insulating polymers. The Constant Voltage Conductivity (CVC) chamber (Figure 1) of the Utah State University Materials Physics Group (USU MPG) has been developed to measure the conductivity of these materials. In this experiment, the CVC chamber was used to simulate the space environment by having the samples in vacuum. This also prevented the materials from being contaminated. Samples of low density polyethylene (LDPE) and Kapton©, or polyimide (PI), were placed between the two parallel plate electrodes while a constant electric field was applied from a battery voltage source (Figure 1, left). From the resulting current, I, the conductivity, σ, was calculated using the expression

$$\sigma = \frac{\vec{J}}{\vec{E}} = \frac{I*d}{V*A} \tag{1}$$

where d is the sample thickness, V is the applied voltage, and A is the electrode area. Lastly, the time-dependent conductivity was fit with a multi-process, physics-based model of time-dependent conductivity to characterize the distribution of atomic-scale defects in the HDIM studied and to evaluate the model itself.

These measurements and analysis provide baseline conductivity and charge decay times useful for determining spacecraft charging effects in materials regularly used in space.

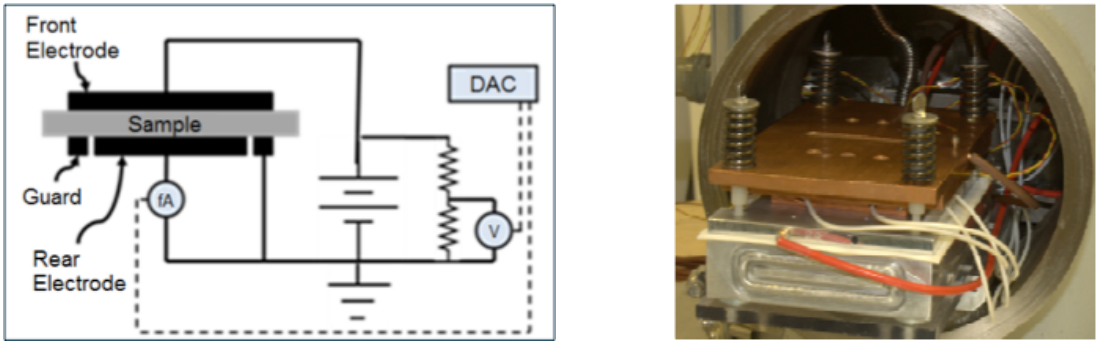

FIG 1. CVC assembly.
Left: Electrical schematic of the CVC chamber.[1]
Right: Picture of CVC chamber.[2]

A. Conductivity Theory and HDIM

Conductivity is the measure of how charge moves through a material under the influence of an electric field. Often this is determined by measuring the current resulting from a voltage applied to the material, using (1) to calculate the material's conductivity. To understand the macroscopic behavior of materials, it is necessary first to understand how the materials behave at the microscopic level. To this end, materials can generally be classified as conductors, semiconductors, and insulators. This classification is based on how charge moves through the material, which is determined by the size of the given material's band gap, or the energy gap between the conduction and valence bands (Figure 2). In insulators, the band gap is large, compared with the thermal energy, so that electrons cannot easily be excited from the valence to the conduction band.

Disordered materials have an amorphous or even semi-crystalline structure, instead of a pure crystalline lattice [3]. Thus, many of the assumptions and resulting properties for crystalline materials (such as long-range order, periodicity, and well-defined band gaps and density of states (DOS)) cannot be directly applied to disordered materials. Disorder can result from many different causes, "including concentrations of impurity atoms, geometric irregularities, the geometry of polymer chains, and their impurities" [4].

Disorder in materials creates a DOS in the band gap, which means it produces localized, or "trap," states of varied energy levels within the gap [4]. So, in disordered materials, electrons can move in the forbidden energy range within the band gap by hopping between these localized states (Figure 2). This movement takes place by primarily two methods: thermally assisted hopping and variable range hopping, or tunneling. This hopping motion of electrons is primarily how charge moves in HDIM [4].

Equation 2 models the time-dependent conductivity in the polymers concerned, with each term modeling a different physical process that dominates in different time intervals [1]:

$$\sigma_{total}(t) = \sigma_{Sat} + \sigma_{pol}^{0} e^{\frac{-t}{\tau_{pol}}} + \sigma_{diff}^{0} t^{-1} + \sigma_{disp}^{0} t^{-(1-\alpha)} \Theta(\tau_{trans} - t) + \sigma_{trans}^{0} t^{-(1+\alpha)} \Theta(t - \tau_{trans}) \qquad (2)$$

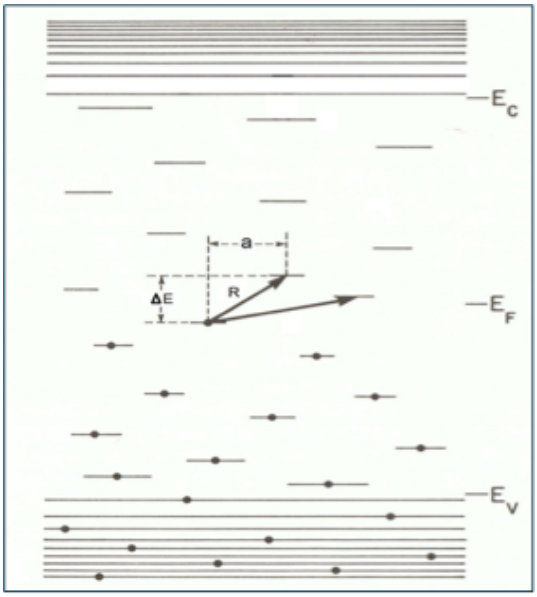

FIG 2. Disordered band structure.[3]

The saturation, or dark, conductivity (σ_{Sat}) is a constant, equilibrium conductivity and is reached at long time scales.

The polarization conductivity (σ_{pol}) is a combination of effects due to the material's response to an applied electric field. This typically dominates for about the first couple minutes or less after the voltage is applied.

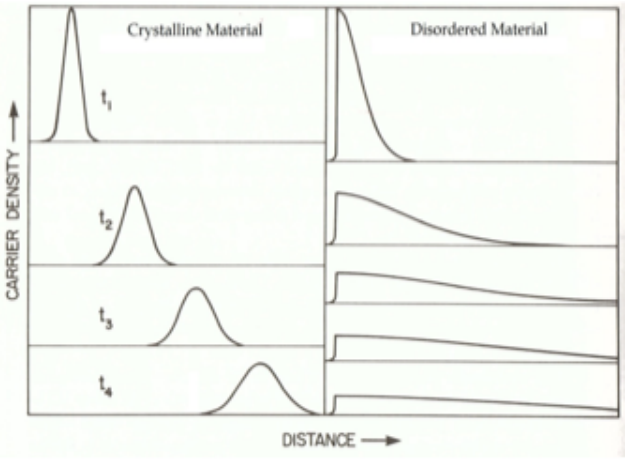

FIG 3. Diffusive versus dispersive transport.[3]

Diffusive conductivity (σ_{diff}) results from normal movement and spreading of the centroid of the charge distribution through the material with time (Figure 3, left). This is typical of charge movement in ordered, or crystalline materials.

Dispersive (σ_{disp}) and transit (σ_{trans}) conductivity both describe the evolving distortion of spatial charge in the material (Figure 3, right). These two terms together are known as dispersive transport and are the mechanisms responsible for charge transport in HDIM, as opposed to diffusive transport. Dispersive conductivity is active before the time $\tau_{transit}$, which is the time when the charge front first reaches the edge of the material. The transit conductivity occurs after $\tau_{transit}$ and until the material reaches equilibrium. The transition between dispersive and transit transport is an abrupt change, or "kink," in the conductivity, as shown in Figure 4.

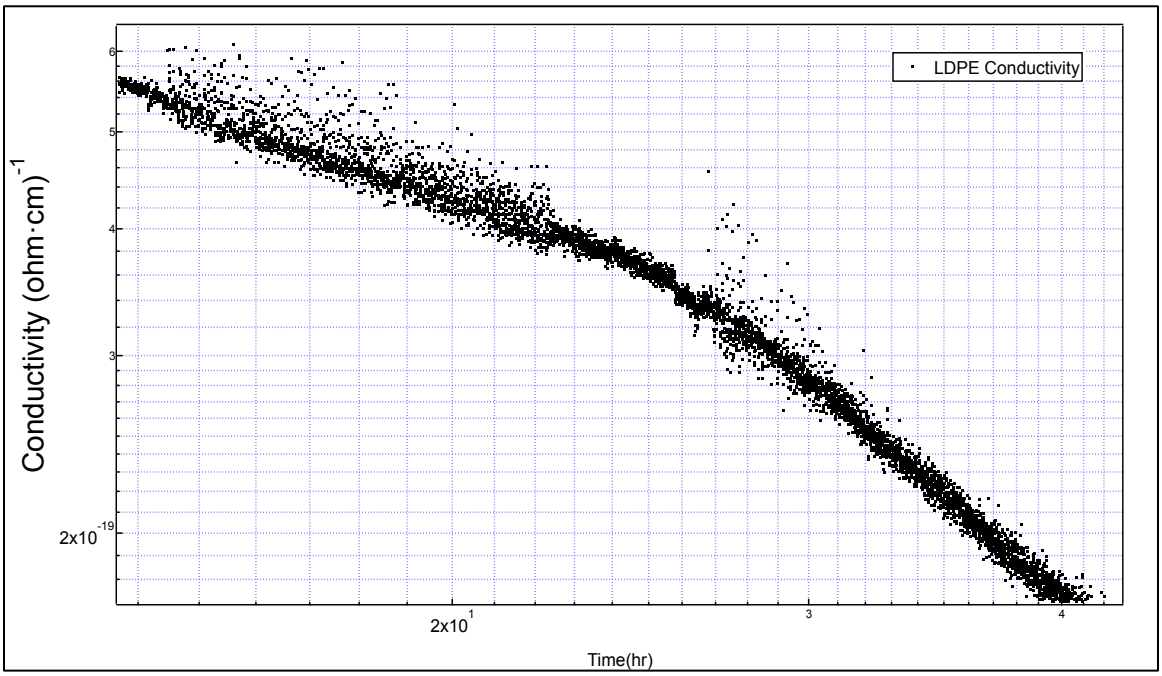

FIG 4. LDPE conductivity versus time: $\tau_{transit}$ zoom after the dark conductivity was subtracted from the LDPE conductivity data (log-log plot).

Figure 3 illustrates diffusive (left) and dispersive (right) transport to compare the two mechanisms. In diffusive transport, the charge front broadens symmetrically and travels intact until it reaches the far side of the sample at the transit time. In dispersive transport however, the charge front distorts asymmetrically and the majority of the charge distribution does not move across the sample. On the contrary, the transit time occurs when the leading edge of the charge distribution reaches the far side of the sample, but a large part of the charge distribution has not moved from its initial position.

Lastly, the parameter α is indicative of the width of trap state energy distribution, i.e. the concentration of states at specific energy levels, which relates to the level of disorder in the material [1]. Because α represents these intrinsic material properties, the theory behind (2) predicts α, in the dispersive and transit terms, will be the same for each material. So, because α should be the same for both dispersive and transit mechanisms, the sum of power law exponents $(1 - \alpha) + (1 + \alpha)$ should be equal to 2; this then is a measure of the viability of (2) based on experimental results [3].

B. CVC Experiment

Conductivity measurements of LDPE and PI were made using the CVC chamber at USU. The CVC chamber has been recently upgraded to make its measurements more precise and increase its capabilites. One of these upgrades is the use of a high voltage battery power supply [2,5]. Using a battery power supply eliminates any alternating displacement current contribution to the conductivity due to the ripple in AC power supplies; this reduces the error in the measured current. This battery supply is comprised of several packs of 9 V batteries connected in series. The individual packs are connected together in series to produce different voltages, depending on what is desired for the material being tested. Because LDPE and PI are both very highly insulating, the high voltages of 420 V and 780 V were used. The current produced by the applied voltage was measured for each material using a Keithley 616 electrometer. This current was recorded and logged with LabView software. Data collection typically lasted until the sample was believed to have reached equilibrium, usually several days, at which time the voltage supply was turned off and the data extracted.

The CVC system at Utah State can measure currents as low as 1×10^{-16} A, or 0.1 fA. However, there is a constant noise, or zero offset, current which is always present due to systematic error in the Keithley 616 electrometer, which records a finite current when no current flows. It is typically ≤ 1 fA and not more than 2.5 fA. This may also include minimal contributions from thermal, radiation, and circuitry effects. When this offset current is subtracted from the data, the resolution is again 0.1 fA. Therefore, the USU CVC system's lowest measureable conductivity is presently as follows: 3×10^{-22} $(\Omega \cdot cm)^{-1}$ at 420 V and 2×10^{-22} $(\Omega \cdot cm)^{-1}$ at 780 V, assuming a typical sample dimension of 27.4 μm thick and 1.9 cm^2 in area.

The battery supply produced the applied voltages shown in Figures 18, 33, and 48. The most unstable region in the applied voltage is the first 16 hr for both

unirradiated PI and radiated PI at 780 V (Figures 18 and 33) and the first 40 hr for LDPE at 420 V (Figure 48). The stability of the battery supply is shown in Table 1, where t_{p0} is the time when the voltage was applied to the sample.

Table 1. Battery voltage source stability.

Sample	Time interval (hr)	Relative uncertainty (%)
Unirradiated PI	t_{p0} - end	0.4
	t_{p0} – 15.8	0.3
	15.8 - end	0.3
Radiated PI	t_{p0} - end	0.4
	t_{p0} – 16.4	0.4
	16.4 - end	0.1
LDPE	t_{p0} - end	0.5
	t_{p0} – 42.7	0.5
	42.7 - end	0.05

The thicknesses of the samples used were as follows: unirradiated PI was 26.0±0.05 μm and 2% systematic uncertainty; radiated PI was 26.3±0.3 μm and 2% systematic uncertainty; and LDPE was 28.3±0.3 μm and 2% systematic uncertainty. The PI and LDPE were both obtained as sheets from GoodFellow. These sheets were then cut to fit on a sample plate (front electrode in Figure 1, left). The samples were prepared by cleaning them with isopropyl alcohol and baking them in the USU bake-out chamber for four days. This chamber heats the samples to approximately 110° C for PI and 65° C for LDPE at vacuum of less than or equal to $1x10^{-6}$ Torr to drive off any moisture or other volatile contaminants. After this, the samples were placed in a nitrogen-filled, enclosed environment until they were placed in the CVC chamber for testing.

Samples of PI were irradiated for a total of 425.34 hr in the USU Space Survivability Test (SST) chamber. The samples were located approximately 10 cm from the Sr^{90} beta radiation source and were irradiated at a dose rate of 0.80±0.02 krad/hr. Thus, the total ionizing dose was 340±5 krad. The samples were removed from the SST chamber four times, three of which were for extended periods (greater than 15 minutes). The samples were kept in a sealed plastic bag to minimize exposure to air during periods when they were not in vacuum. When the samples were outside the chamber for extended periods and when they were removed for the final time, they were placed in a nitrogen-filled, enclosed environment. The PI sample was in the nitrogen-filled environment for 17.8 days ±0.1 hr following irradiation and prior to conductivity tests.

II. RESULTS

Having obtained the current versus time data for unirradiated PI, radiated PI, and LDPE, the conductivity was calculated and graphed in Igor Pro. The measured

current data were adjusted to remove a constant zero offset current. The zero offset, or background, current was measured prior to applying the voltage by allowing time for the sample to show a steady, equilibrium current without any applied voltage. This offset current was later calculated and subtracted from the data in Igor Pro. The conductivity versus time curve was then fit with the model in (2) to determine the viability of the model and underlying theory. Also, the conductivity data were smoothed in Igor Pro using a box algorithm. PI and radiated PI were averaged using 200 data points (250 s) and LDPE using 100 data points (120 s), respectively. Using this many points to average these data is justified because LabView recorded a data point approximately every 1.5 s. The shortest data collection time was 107.8 hr, or about 3.9×10^5 s. This correlates to roughly 2.6×10^5 data points for the shortest run. However, smoothing conductivity data is not justified in the polarization region (about the first 150 s after the voltage is applied), because this region contains only around 50 to 100 data points and the current is changing rapidly.

The precision of time measurements were on the order of ±0.1 s. Except for the first few data points related to polarization, the uncertainties in time were negligible, smaller than the width of the data points. Random error in the current measurements was determined by the method in [5] and calculated in Igor Pro. There was also a systematic error of ±5% in current measurements due to the Keithley 616 electrometer. Short-term transients in current, particularly evident at low currents (see Figure 8) are due to external stimuli, such as motion in the room. The area uncertainty was 1.9±0.02 cm^2 (±1%) and ±4% systematic uncertainty. Systematic errors in area are dominated by uncertainties in the contact area and the effective electrode area [1]. The uncertainties in sample thicknesses were as follows: unirradiated PI was 26.0±0.5 μm (±2%) and 2% systematic uncertainty; radiated PI was 26.3±0.3 μm (±1%) and 2% systematic uncertainty; and LDPE was 28.3±0.3 μm (±1%) and 2% systematic uncertainty. The random errors in the applied voltage for each material are listed in Table 1 as the relative uncertainty in the applied voltage from when the voltage was applied (t_{p0}) to the end of data collection. Systematic uncertainties in voltage were negligible. The random error in the dark conductivity, in accord with [5], was calculated by addition in quadrature of the random errors in current, voltage, thickness, and area. This yielded a precision of 2% for unirradiated PI, radiated PI, and LDPE. The accuracy in dark conductivity for unirradiated PI, radiated PI, and LDPE was 11%. This was calculated by addition of the systematic uncertainties in current, voltage, thickness, and area; this is dominated by the systematic uncertainties in current and area.

The percent fractional residual of the conductivity model (2) was calculated from the following equation:

$$\left[\frac{(\sigma(t)_{fit}-\sigma(t)_{data})}{\sigma(t)_{fit}}\right] * 100\% \qquad (3)$$

This was then plotted to show how well the model fit the conductivity data.

The uncertainty in the transit time, $\tau_{transit}$, was determined by finding the width of the curve, or kink, in the data around the transit time. This curve was most distinct when the dark conductivity had been subtracted from the conductivity data (Figure 4). For the other fitting parameters, the uncertainty was determined by the

finding the change in the parameter that produced a ±10% difference in the appropriate percent fractional residual plot. The different parameters fit were as follows: $\tau_{transit}$, α_{disp}, α_{trans}, σ_{Sat}, σ^0_{pol}, σ^0_{disp}, σ^0_{trans}, and τ_{pol} (for three-polarization fits the polarization terms became $\sigma^0_{pol\_1}$, $\sigma^0_{pol\_2}$, $\sigma^0_{pol\_3}$, τ_{pol_1}, τ_{pol_2}, and τ_{pol_3}). The parameters, with their error, are listed in Table 2. Also listed is t_{P0}, the time when the voltage was applied to the sample. It should be noted that the following figures begin at approximately t_{P0}, not the time when data started being recorded for each sample.

Table 2. Modeled conductivity parameters.

Parameter	**Unirradiated PI**		**Radiated PI**		**LDPE**
	1-pol	3-pol	1-pol	3-pol	1-pol
$\sigma^0_{pol\_1}$	(1.8±0.8)x10^{-18}	(1.8±0.7)x10^{-18}	(4±3)x10^{-19}	(1±3)x10^{-18}	(2±10)x10^{-17}
$\sigma^0_{pol\_2}$		(9±3)x10^{-18}		(7±2)x10^{-18}	
$\sigma^0_{pol\_3}$		(6±3)x10^{-17}		(7±2)x10^{-17}	
σ^0_{disp}	(1.1±0.2)x10^{-19}		(1.5±0.2)x10^{-19}		(1.6±0.6)x10^{-18}
σ^0_{trans}	(3.0±0.6)x10^{-18}		(4.7±0.8)x10^{-18}		(5±2)x10^{-17}
σ_{Sat} (Ω•cm)$^{-1}$	(1.34±0.03)x10^{-20}		(2.07±0.04)x10^{-20}		(8.3±0.2)x10^{-19}
t_{P0} (hr)	0.1504		0.26523		0.75833
τ_{pol_1}	(9±3)x10^{-3}	(9±3)x10^{-3}	(4±2)x10^{-2}	(2.2±0.8)x10^{-2}	(1±2)x10^{-3}
τ_{pol_2}		(2.3±0.5)x10^{-3}		(3.6±0.7)x10^{-3}	
τ_{pol_3}		(0.7±0.1)x10^{-3}		(6.0±0.8)x10^{-4}	
$\tau_{transit}$ (hr)	40±2		25±1		25.8±0.4
α_{disp}	0.49±0.04		0.57±0.05		0.5±0.1
α_{trans}	0.40±0.06		0.50±0.05		0.5±0.1
$(1-\alpha_{disp})+(1+\alpha_{trans}) = 2+(\alpha_{trans}-\alpha_{disp})$	1.9±0.1		1.9±0.1		2.0±0.2

A. Unirradiated PI

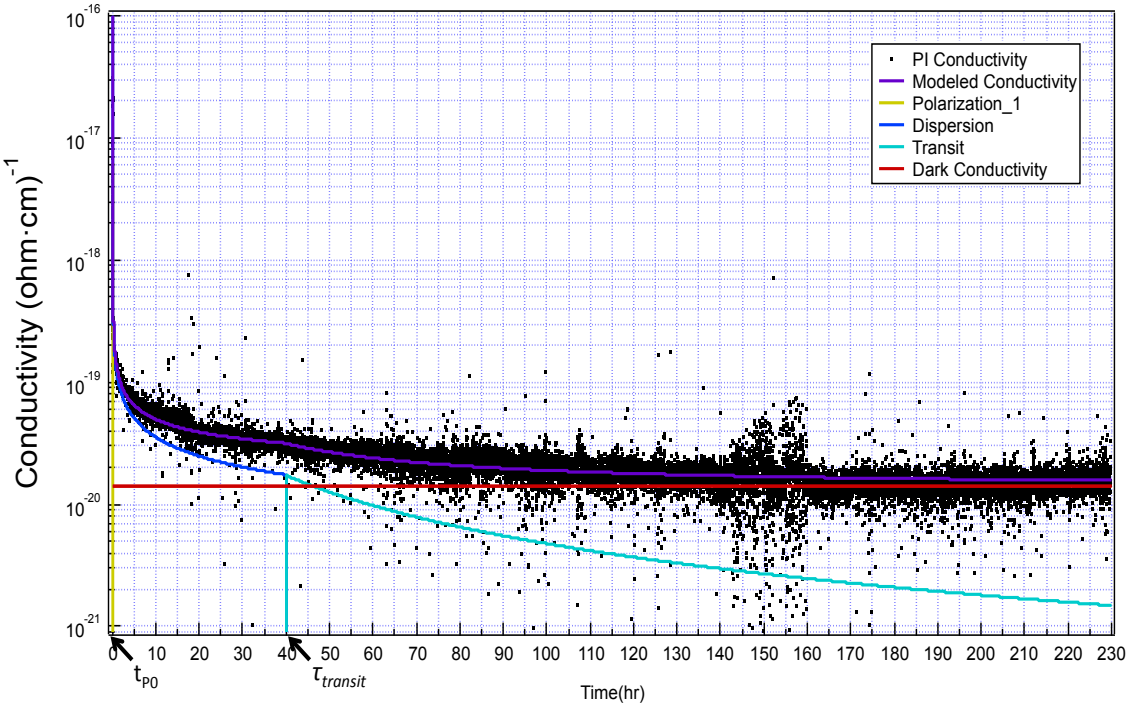

FIG 5. Unirradiated PI conductivity (one-polarization fit) versus time: log-linear plot.

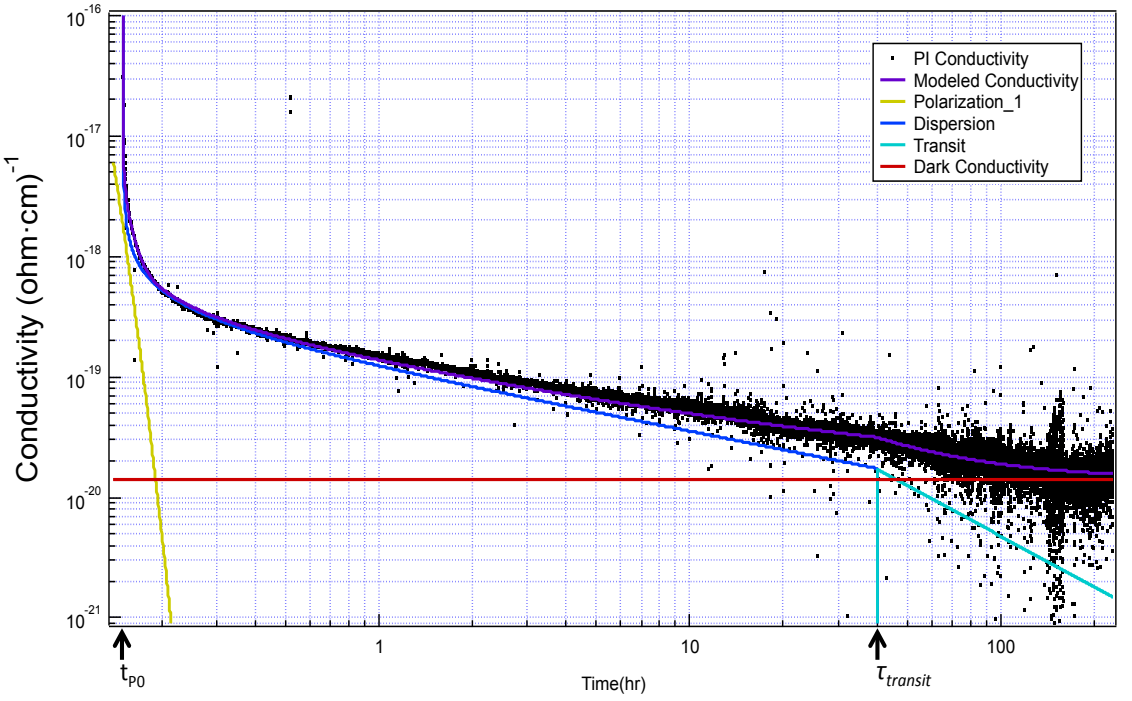

FIG 6. Unirradiated PI conductivity (one-polarization fit) versus time: log-log plot.

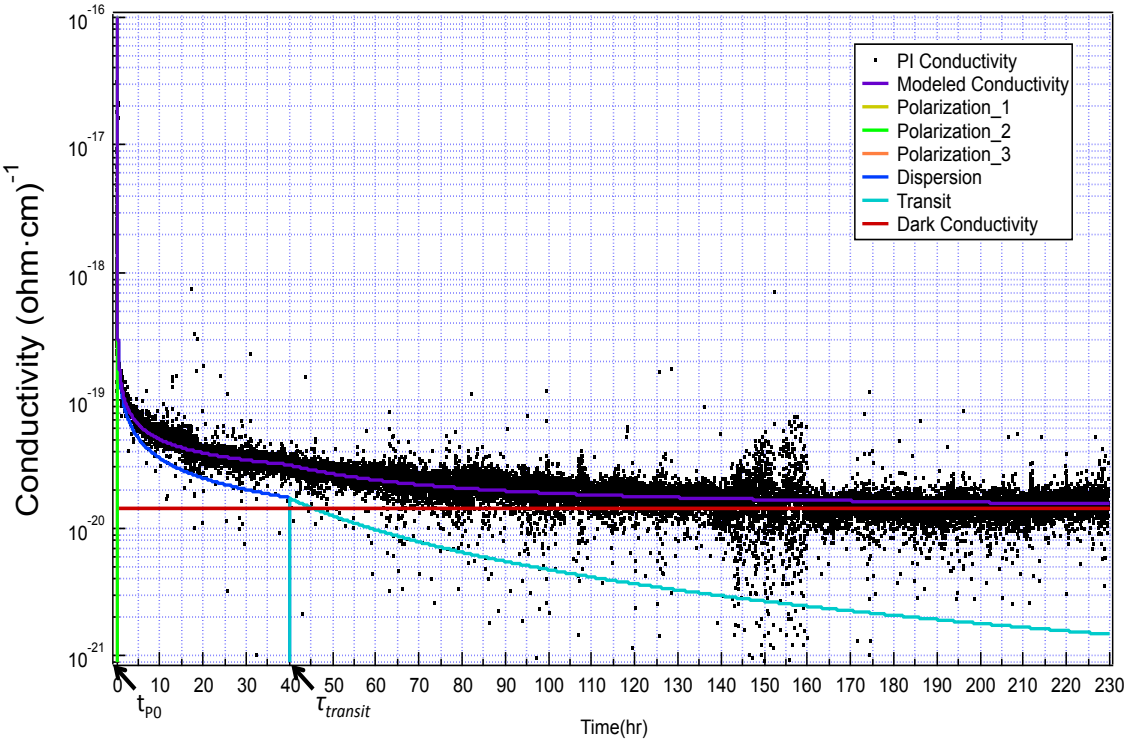

FIG 7. Unirradiated PI conductivity (three-polarization fit) versus time: log-linear plot.

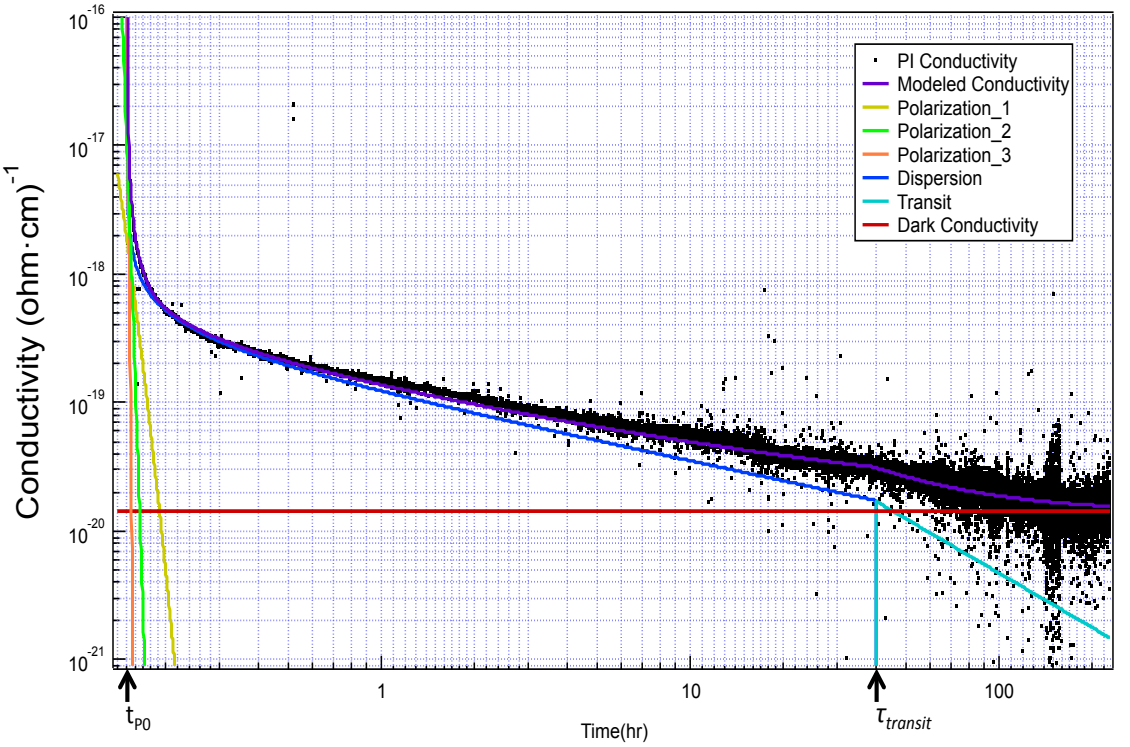

FIG 8. Unirradiated PI conductivity (three-polarization fit) versus time: log-log plot.

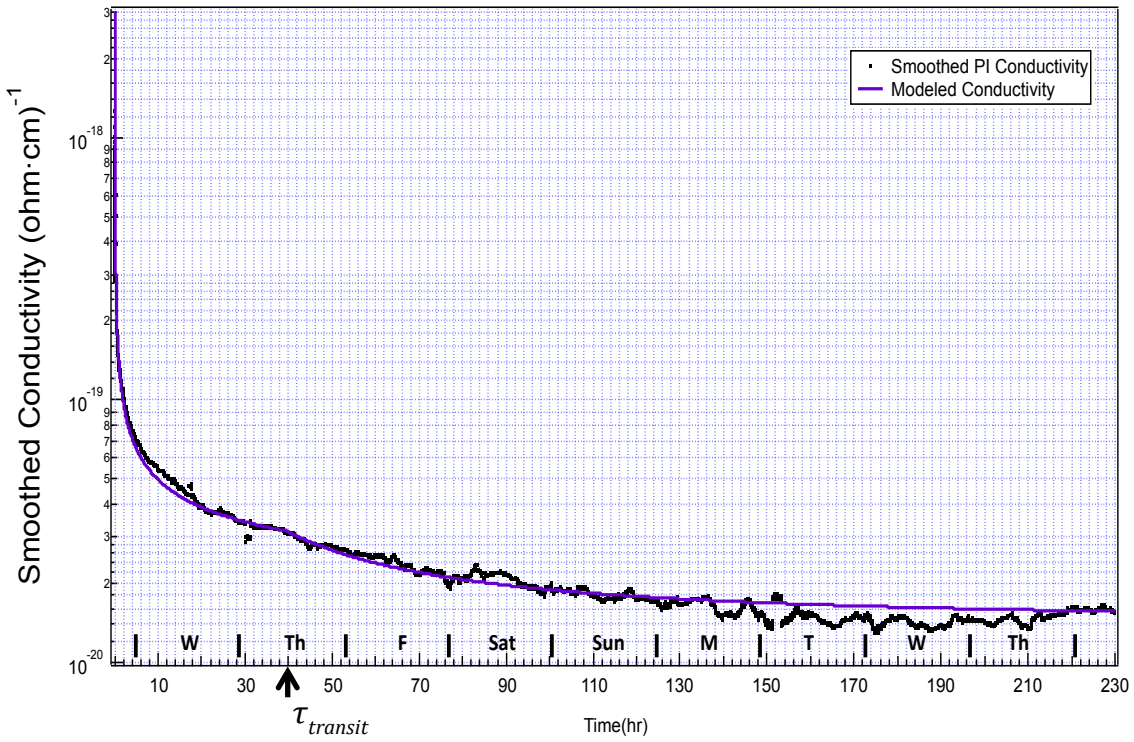

FIG 9. Smoothed unirradiated PI conductivity (one-polarization fit) versus time: log-linear plot.

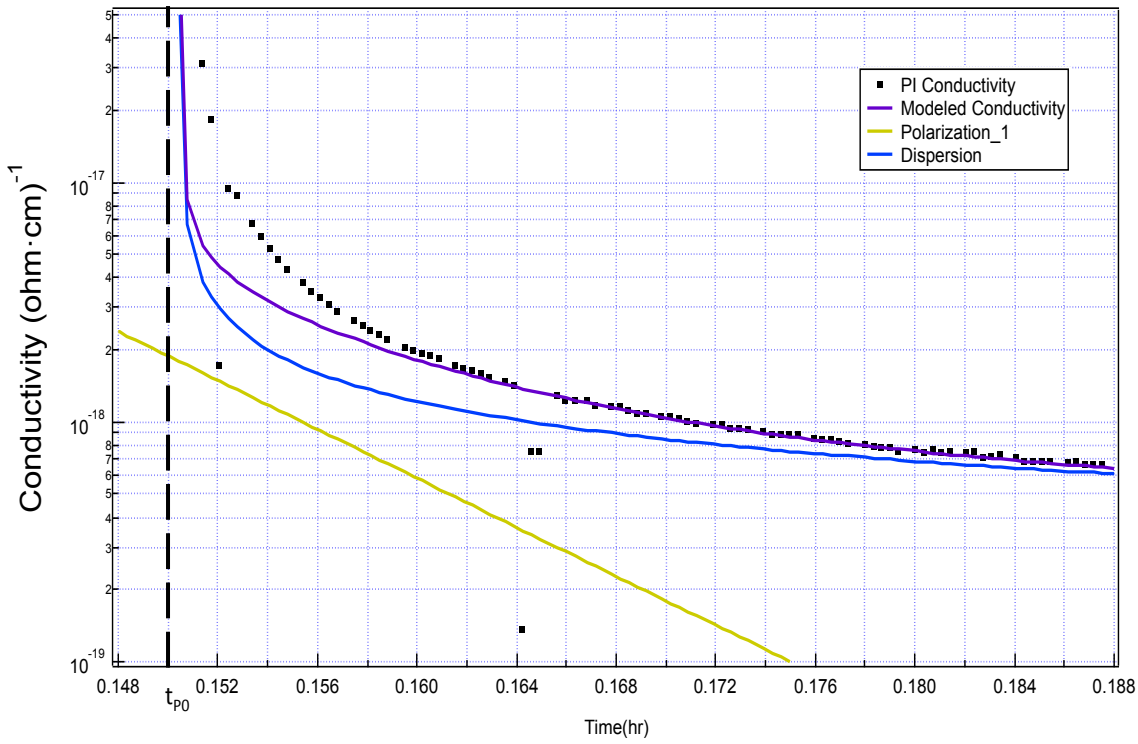

FIG 10. Unirradiated PI conductivity (polarization zoom and one-polarization fit) versus time: log-linear plot.

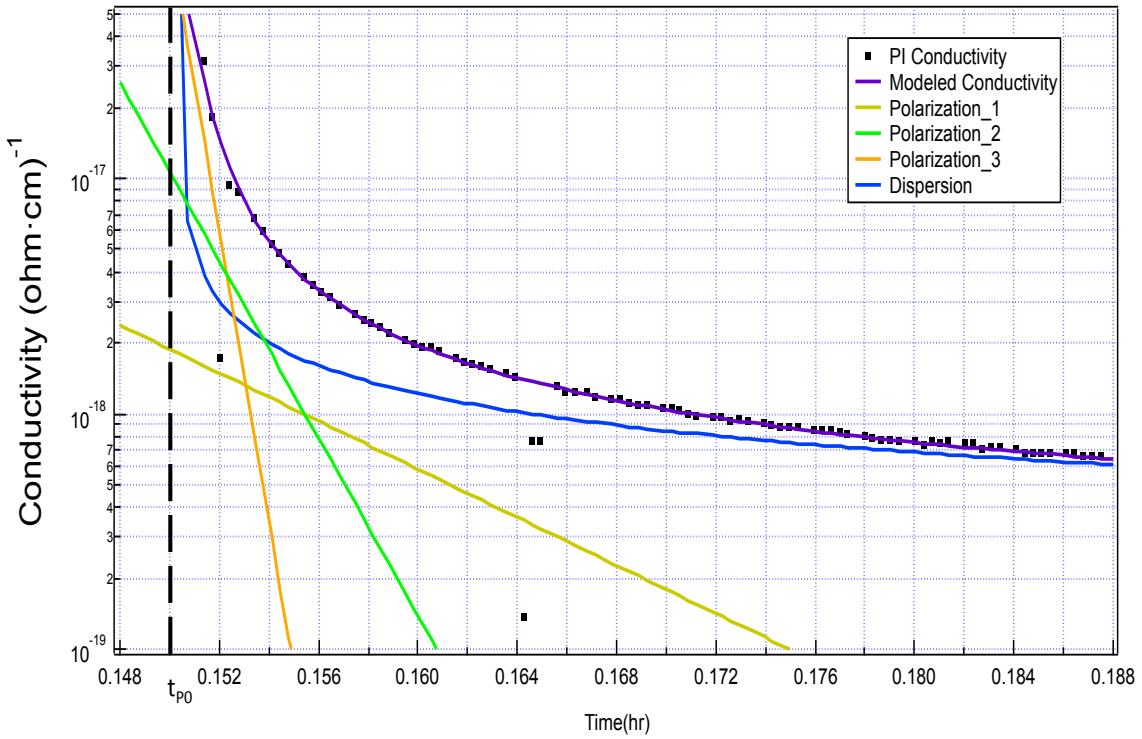

FIG 11. Unirradiated PI conductivity (polarization zoom and three polarization fit) versus time: log-linear plot.

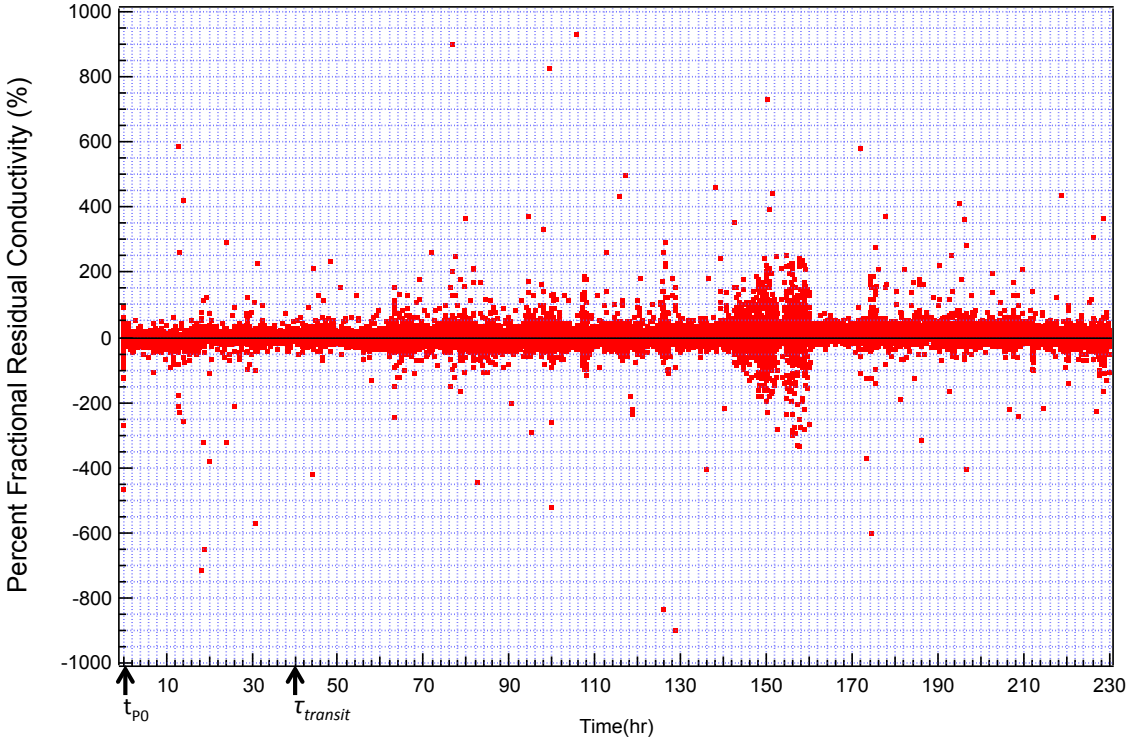

FIG 12. Percent fractional residual one-polarization unirradiated PI conductivity versus time: linear-linear plot.

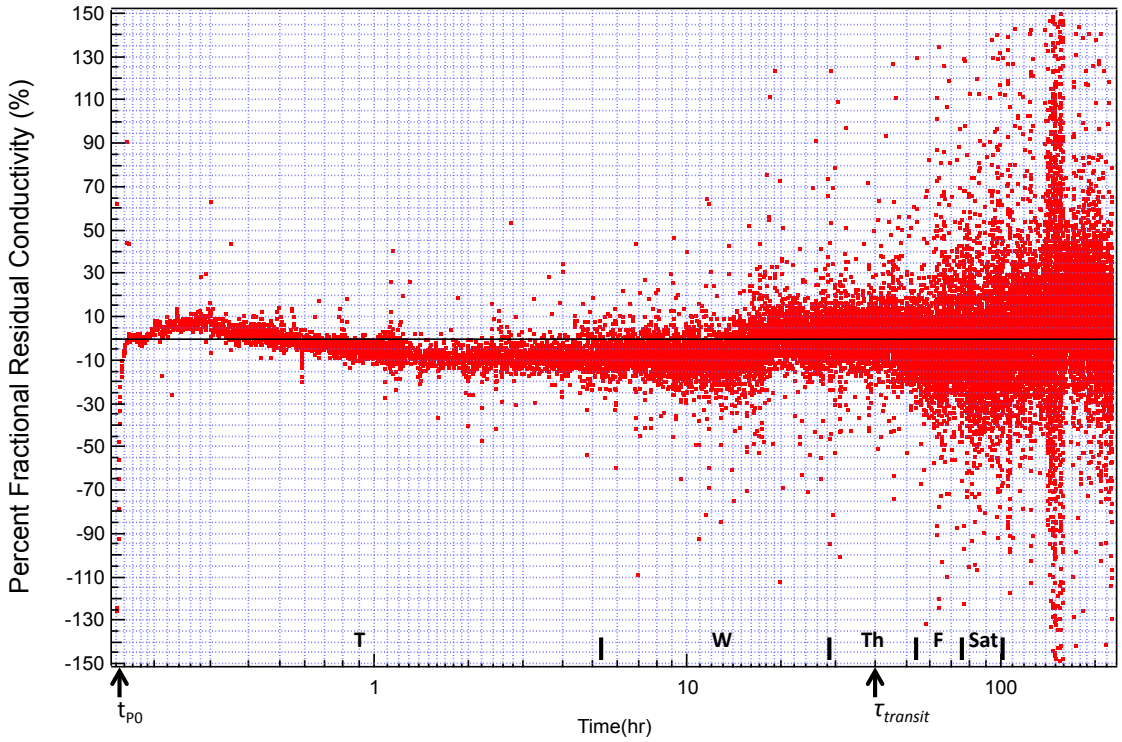

FIG 13. Percent fractional residual one-polarization unirradiated PI conductivity versus time: linear-log plot.

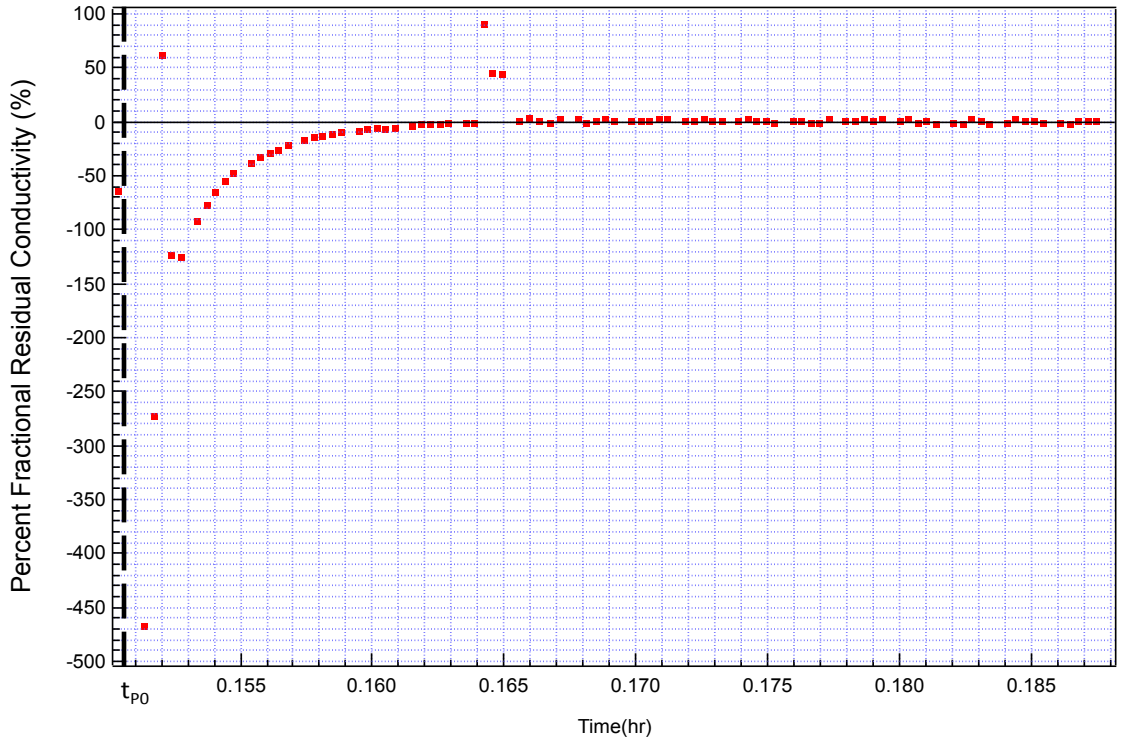

FIG 14. Percent fractional residual one-polarization unirradiated PI conductivity (polarization zoom) versus time: linear-linear plot.

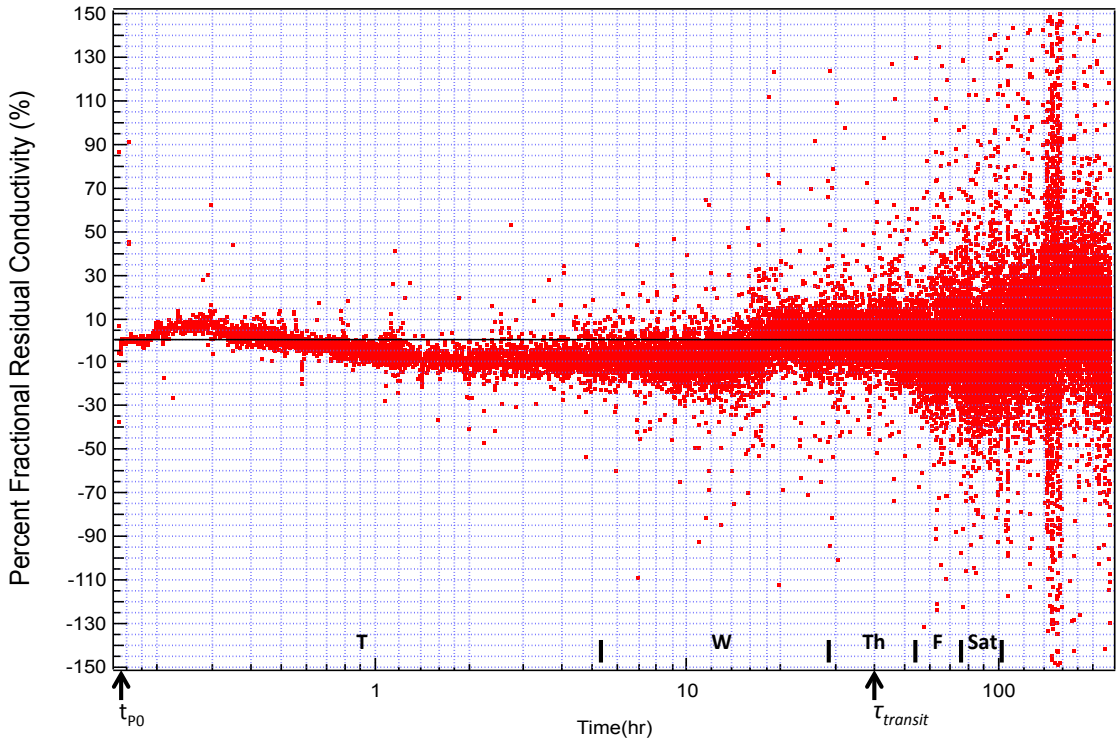

FIG 15. Percent fractional residual three-polarization unirradiated PI conductivity versus time: linear-log plot.

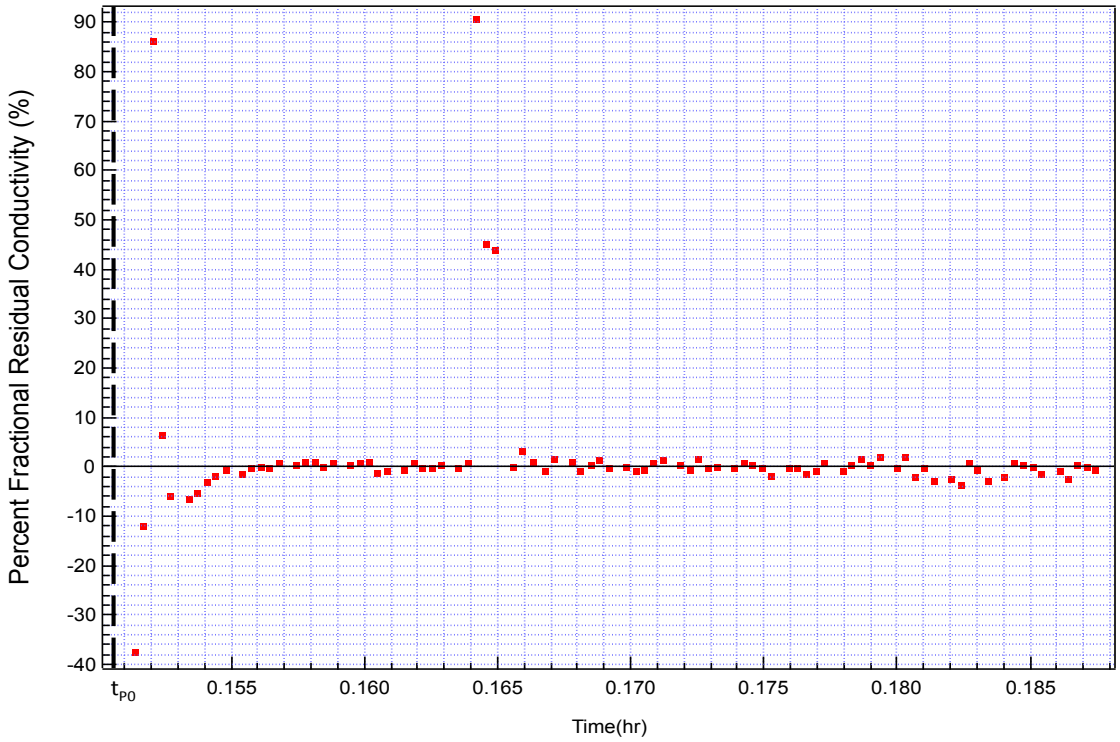

FIG 16. Percent fractional residual three-polarization unirradiated PI conductivity (polarization zoom) versus time: linear-linear plot.

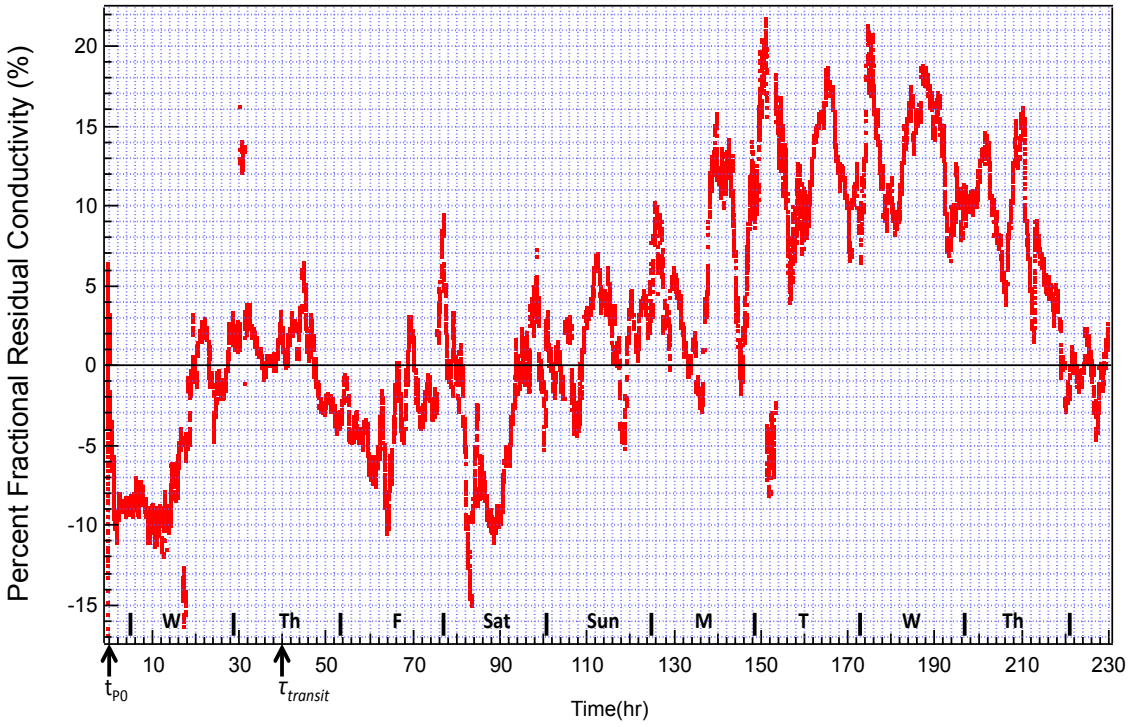

FIG 17. Percent fractional residual one-polarization smoothed unirradiated PI conductivity versus time: linear-linear plot.

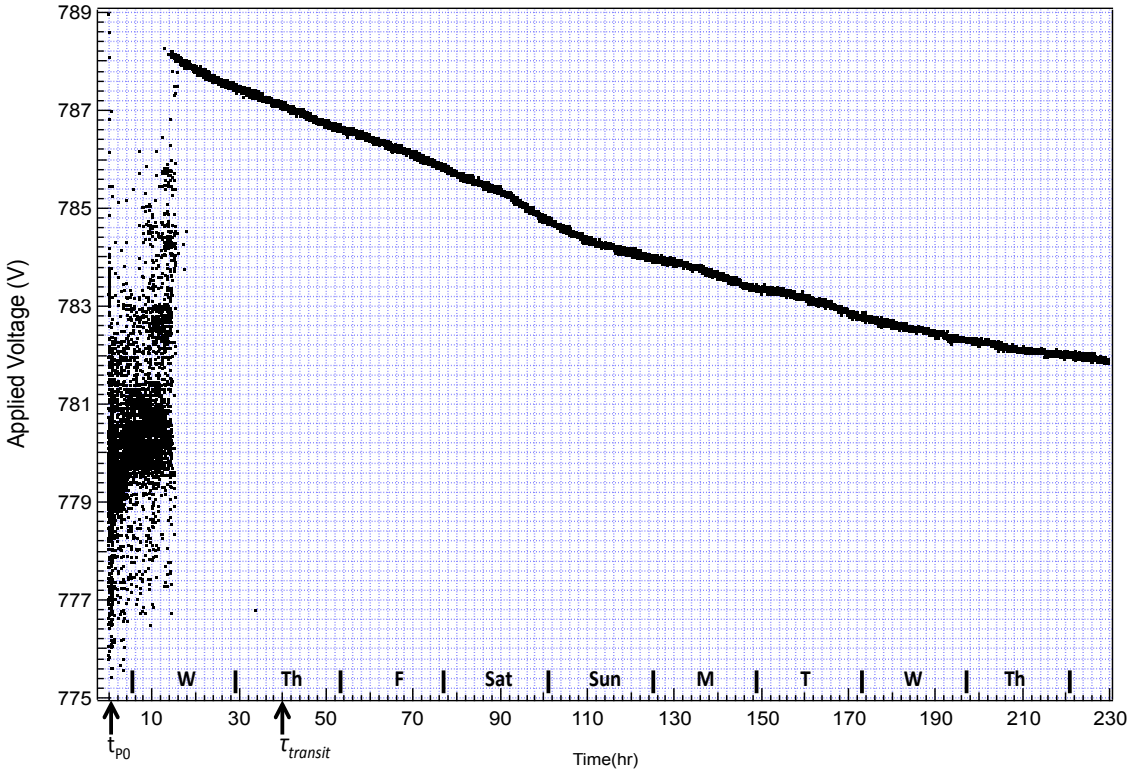

FIG 18. Unirradiated PI applied voltage versus time.

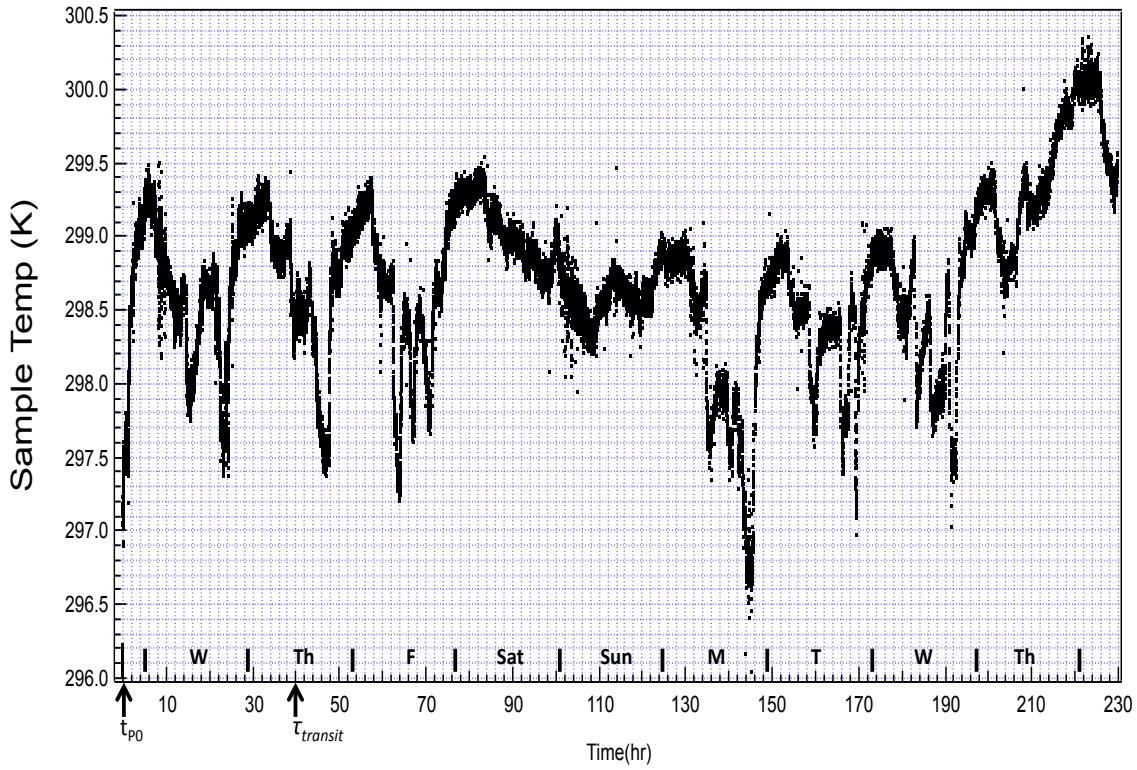

FIG 19. Unirradiated PI sample temperature versus time.

The unirradiated PI conductivity data were later fit using a model that included three polarization terms. The resulting conductivity equation is

$$\sigma_{total}(t) = \sigma_{Sat} + \sigma^0_{pol\,1} e^{-\frac{t}{\tau_{pol\,1}}} + \sigma^0_{pol\,2} e^{-\frac{t}{\tau_{pol\,2}}} + \sigma^0_{pol\,3} e^{-\frac{t}{\tau_{pol\,3}}} + \sigma^0_{diff} t^{-1} + \sigma^0_{disp} t^{-(1-\alpha)} \Theta(\tau_{trans} - t) + \sigma^0_{trans} t^{-(1+\alpha)} \Theta(t - \tau_{trans}) \quad (4)$$

Figures 5 through 11 are graphs of unirradiated PI conductivity versus time. They include the modeled conductivity fit using (2) and (4) for one-polarization (Figures 5, 6, and 10) and three-polarization (Figures 7, 8, and 11) term fits, and the individual contributions of the constituent terms: polarization, dispersion, transit, and dark conductivity. Figures 10 and 11 are log-linear plots of the polarization region of the conductivity data, or about the first 150 s after t_{p0} (approximately 0.15-0.188 hr). Figures 12 through 17 are plots of the percent fractional residual conductivity versus time. Figure 9 is a graph of the smoothed PI conductivity versus time and its corresponding percent fractional residual plot is Figure 17. For Figure 9, the conductivity data were averaged over 200 data points. Figure 18 is a graph of the applied voltage versus time for this data set and Figure 19 is the sample temperature versus time. After the first sixteen hours, Figure 18 shows a linear drift in the voltage (due to battery discharge) of about 31 mV/hr. This systematic effect is canceled out in the conductivity calculation. Figure 12 is included for completeness

to show how well all the data collected are fit by (2). Table 2 contains the parameters resulting from fitting the PI data with (2) and (4).

Referring to Figures 6 and 8, it is apparent that the data for unirradiated PI conductivity is fit well by both (2) and (4). Even after $\tau_{transit}$, the percent error for the majority of data points is ±50% (Figure 13 for (2) and Figure 15 for (4)). Also, the difference between fitting the unirradiated PI data with (2) and (4) is only apparent in the initial minutes after the voltage is applied (the first 0.1hr in Figures 13 and 15). Because the smoothed conductivity does not accurately show the rapidly changing polarization region, Figures 14 and 16 provide an analysis for the fits of (2) and (4) which show that the polarization part of the unirradiated PI data is fit by (4) to within ±4% for a majority of data points (Figure 16). Using two polarization terms was attempted, but it was found that this left data points out of the fitting that could be included by using a third polarization term. From Figure 17 it is evident that both (2) and (4) fit, for the majority of the data, to less than +25% and -20%. There appear to be two classes of agreement with the modeled conductivity. One is short-term variations (on the order of minutes to hours); this is small, on the order of 2-3%, with longer variations on the order of tens of hours being ±5-10% (Figure 17). Figure 17 also shows an even longer trend (see 80 hr to 220 hr) that is ±20%. The longer trend may be due to systematic errors such as temperature or current zero drifts.

Areas where the percent fractional residual plots (e.g. Figure 17) are positive correspond to the modeled conductivity over-predicting the unirradiated PI conductivity data. This is illustrated by Figure 17 in the region from 120-220 hr. Conversely, where the percent fractional residual plot is negative corresponds to areas where the modeled conductivity under-predicts the data. Figure 17, in the region from 50-65 hr shows this. Also, Figure 14 shows that (2) under-predicts the PI conductivity data in the polarization region.

Figure 18 shows the cyclic behavior of the temperature of the sample plate in the CVC chamber (Figure 1). This corresponded to temperature cycles of the room where the CVC chamber is located, which was not measured but conjectured based on the experience of the experimenters in the room. As shown in Figure 19, this behavior has roughly 24 hr cycles, with maxima alternating with minima about every 12 hr in the approximate regions 1-80 hr and 130-230 hr. The exception is the region from about 80-130 hr in Figure 18. This roughly 48 hr span was a weekend, when the temperature of the room was more constant due to the door of the room staying closed for two days.

B. Radiated PI

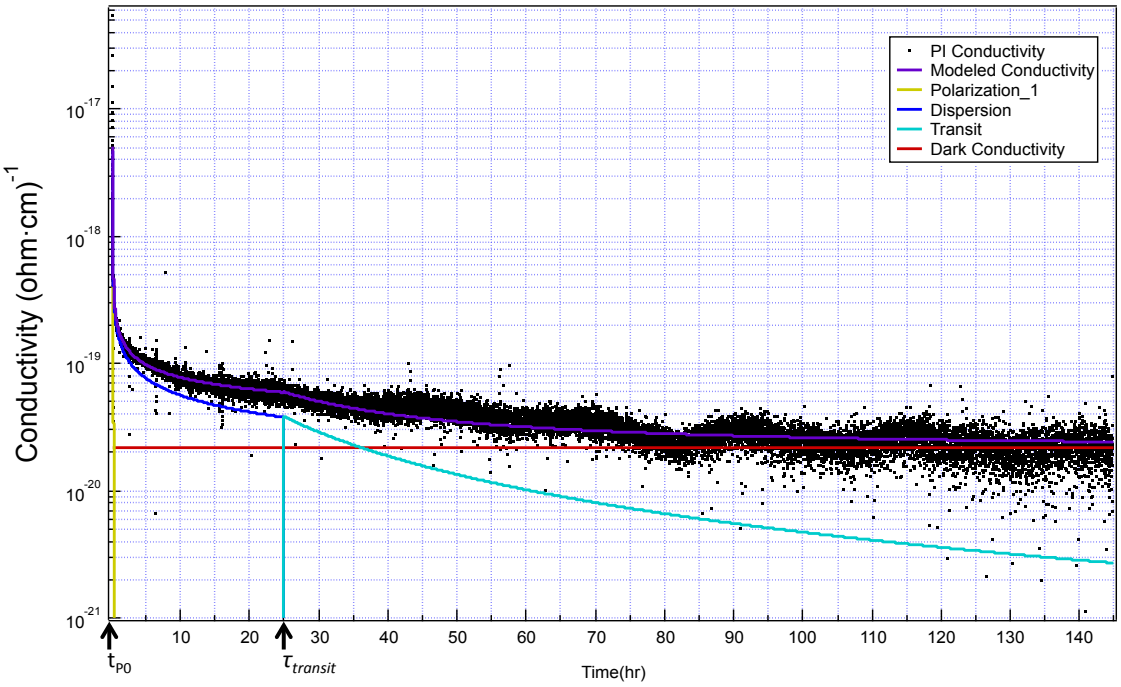

FIG 20. Radiated PI conductivity (one-polarization fit) versus time: log-linear plot.

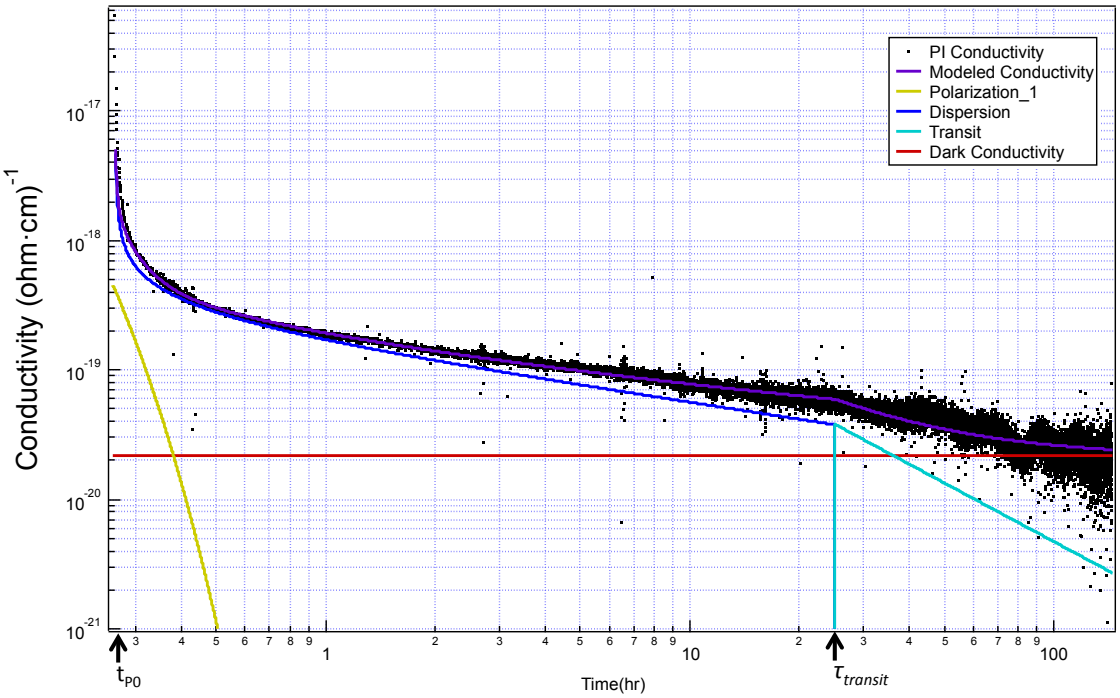

FIG 21. Radiated PI conductivity (one-polarization fit) versus time: log-log plot.

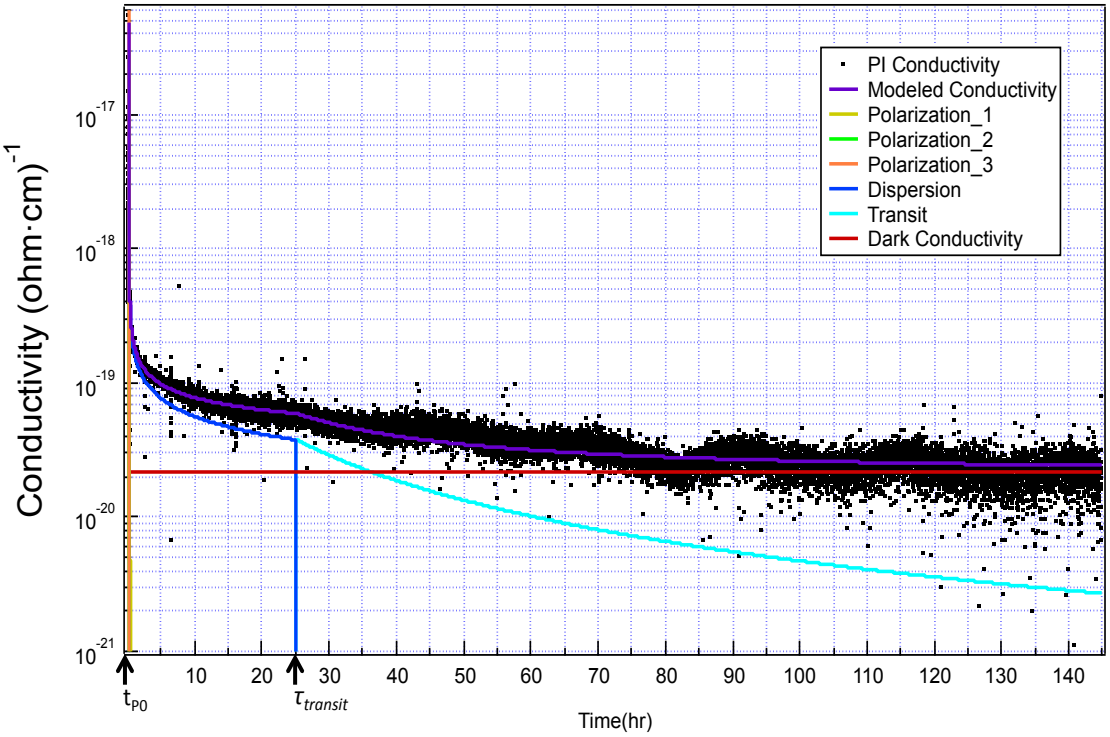

FIG 22. Radiated PI conductivity (three-polarization fit) versus time: log-linear plot.

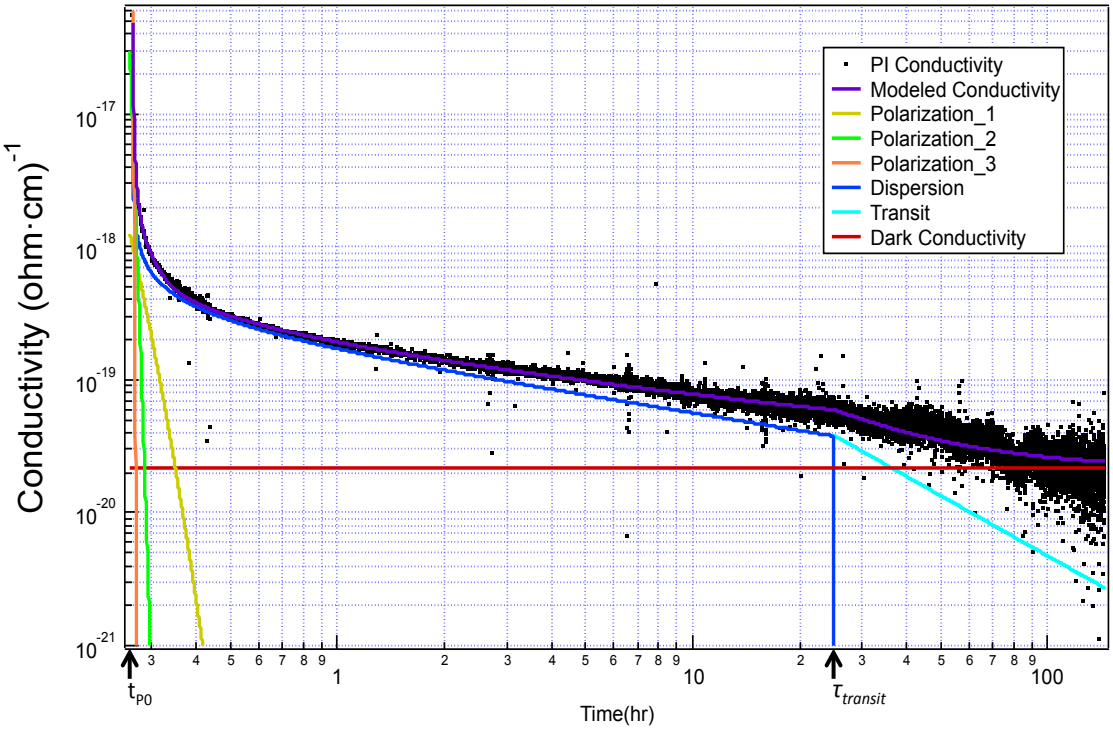

FIG 23. Radiated PI conductivity (three-polarization fit) versus time: log-log plot.

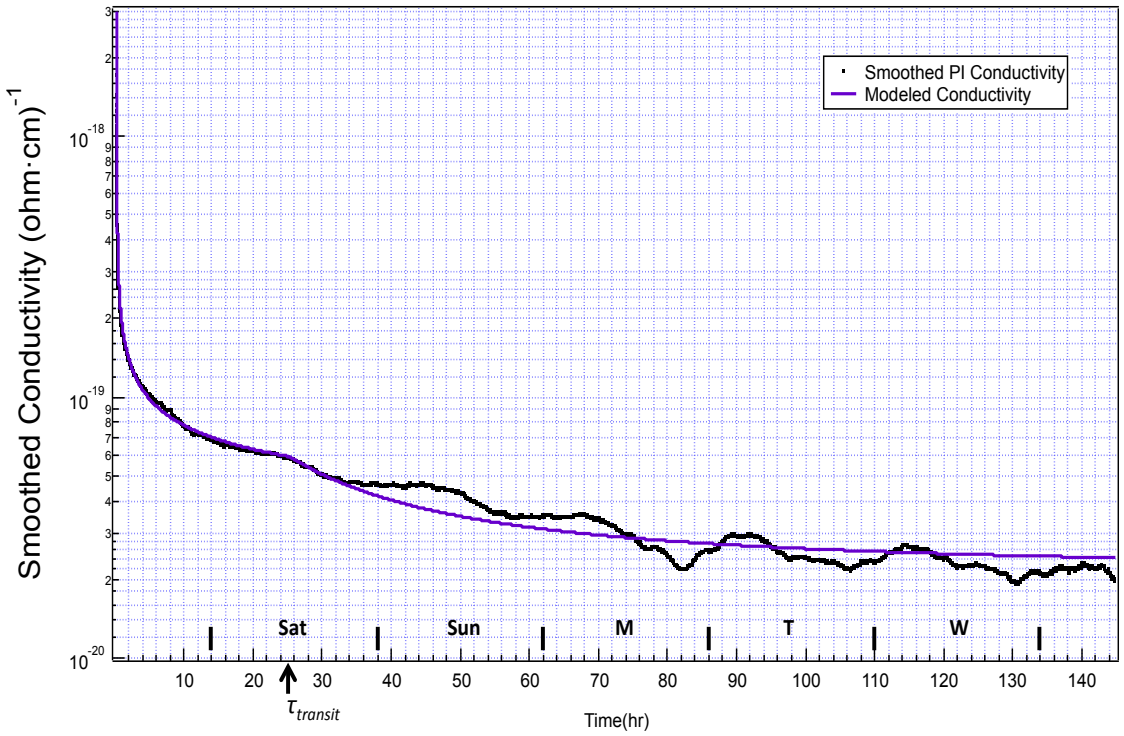

FIG 24. Smoothed radiated PI conductivity (one-polarization fit) versus time: log-linear plot.

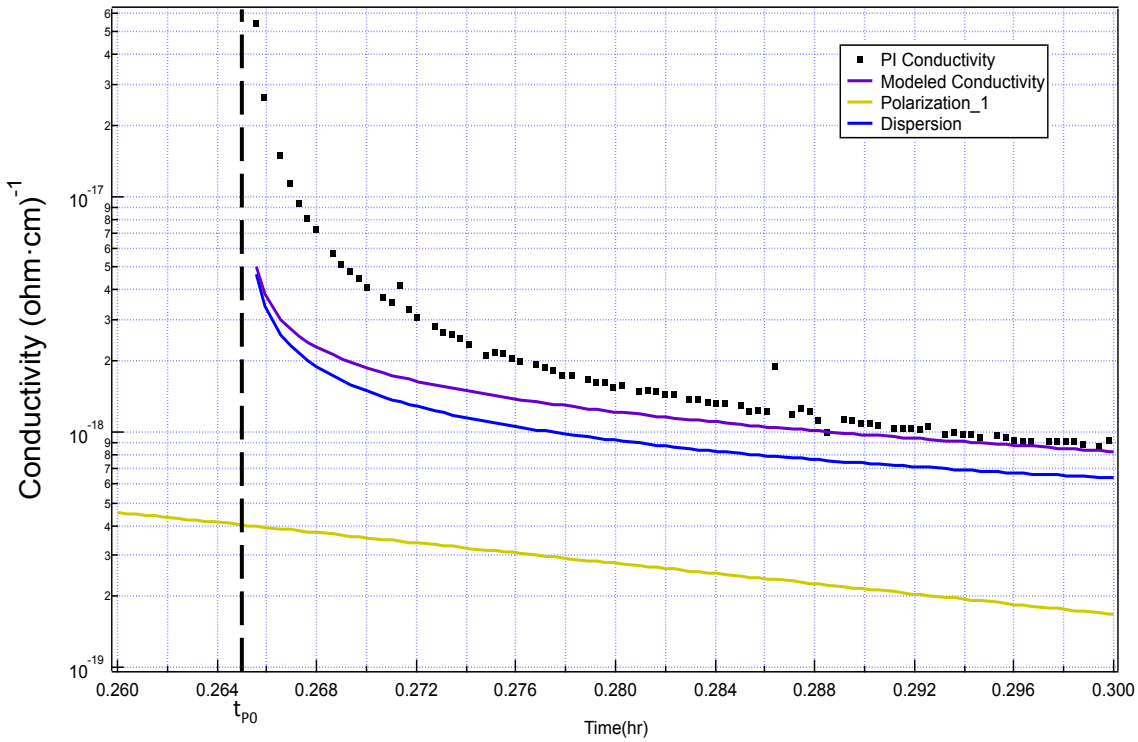

FIG 25. Radiated PI conductivity (polarization zoom and one-polarization fit) versus time: log-linear plot.

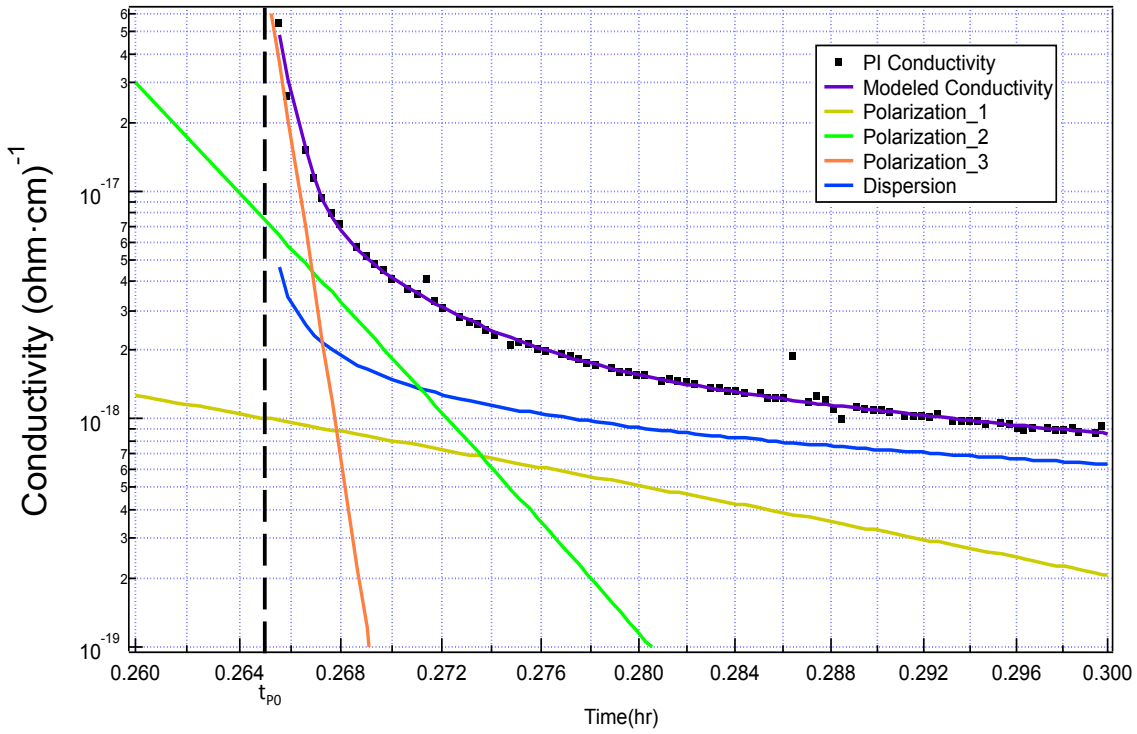

FIG 26. Radiated PI conductivity (polarization zoom and three polarization fit) versus time: log-linear plot.

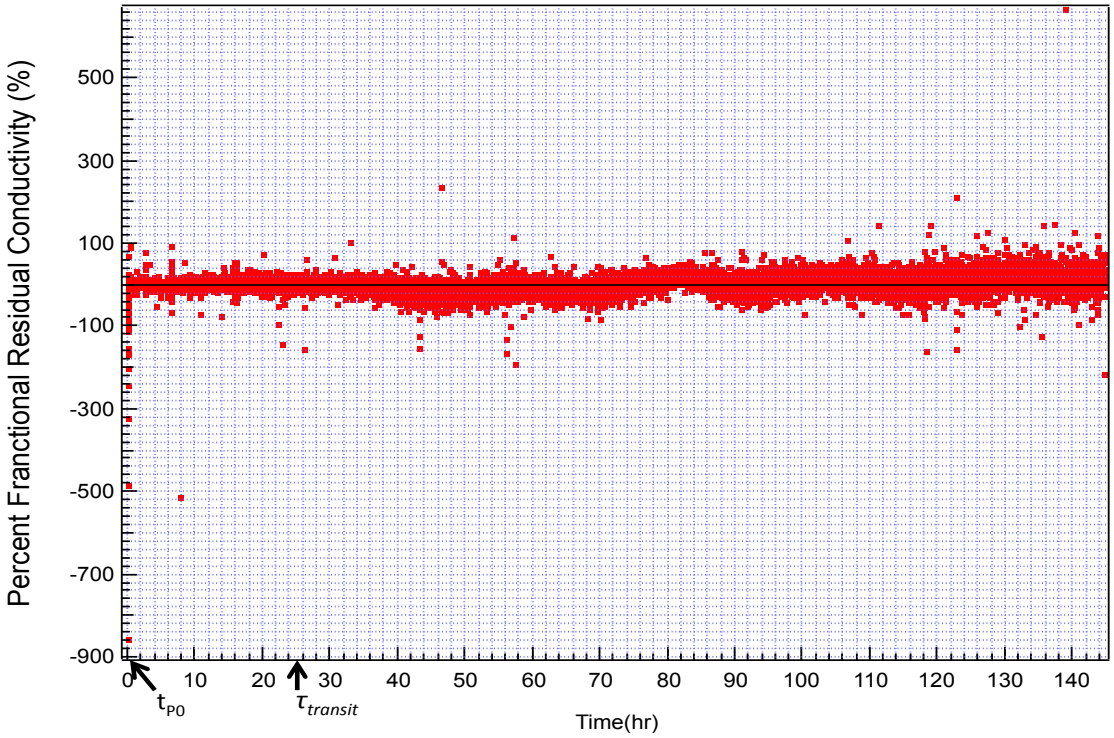

FIG 27. Percent fractional residual one-polarization radiated PI conductivity versus time: linear-linear plot.

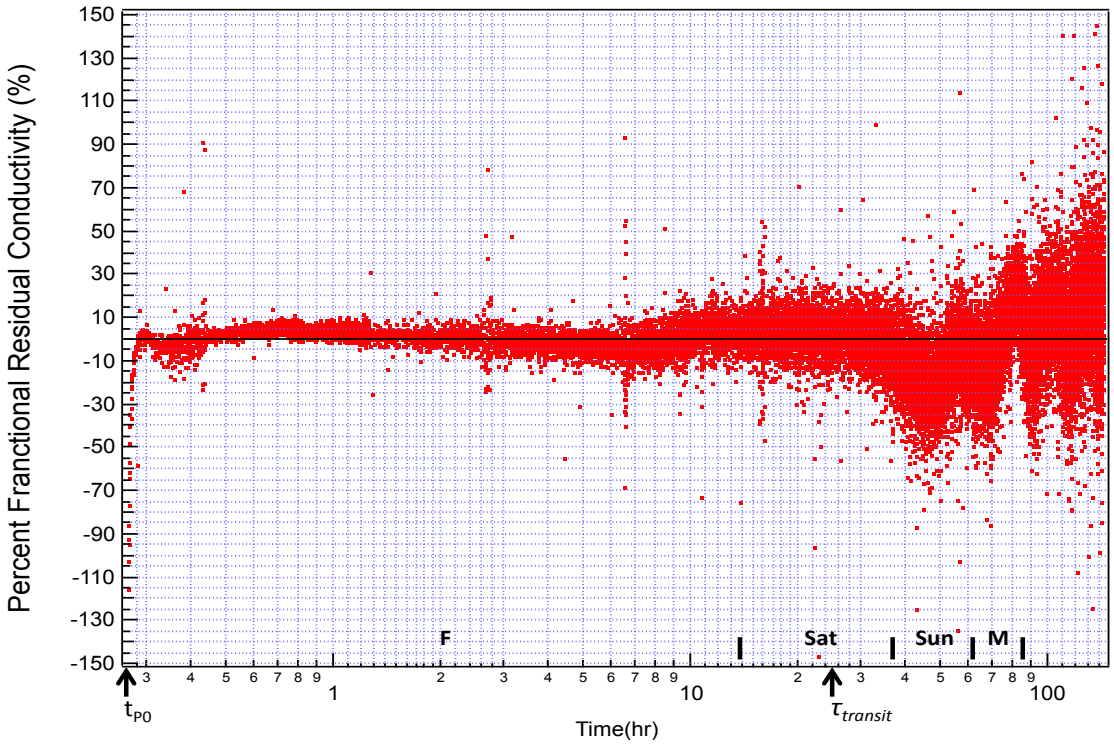

FIG 28. Percent fractional residual one-polarization radiated PI conductivity versus time: linear-log plot.

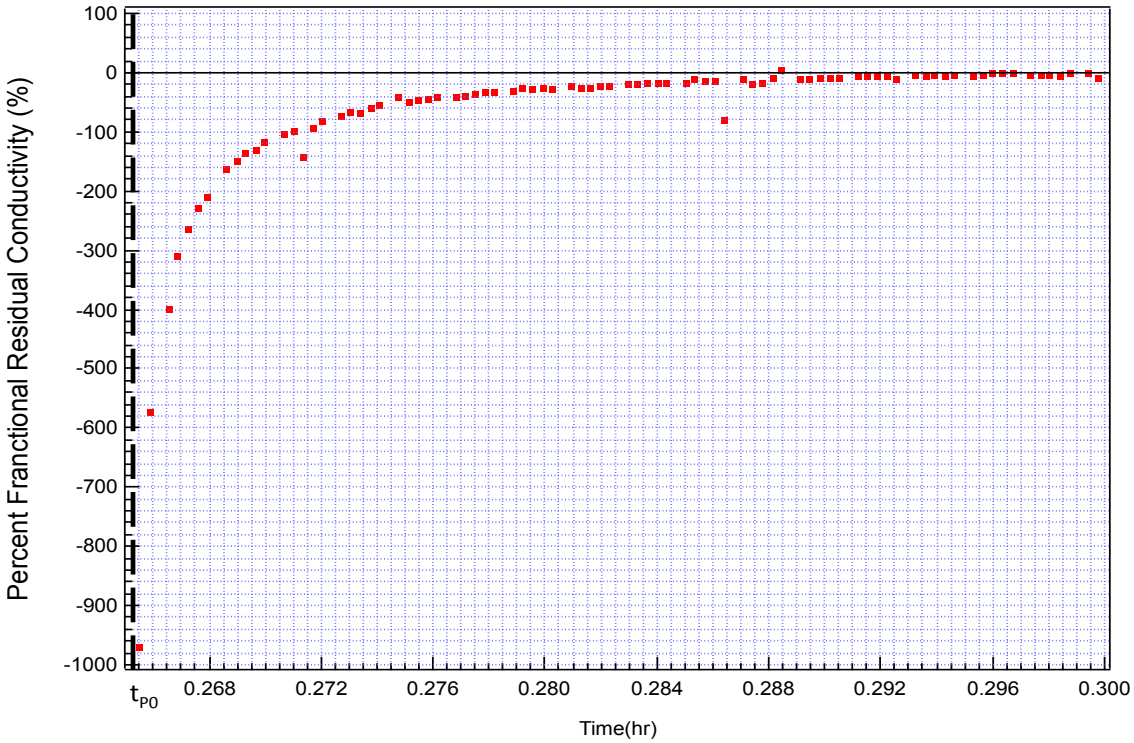

FIG 29. Percent fractional residual one-polarization radiated PI conductivity (polarization zoom) versus time: linear-linear plot.

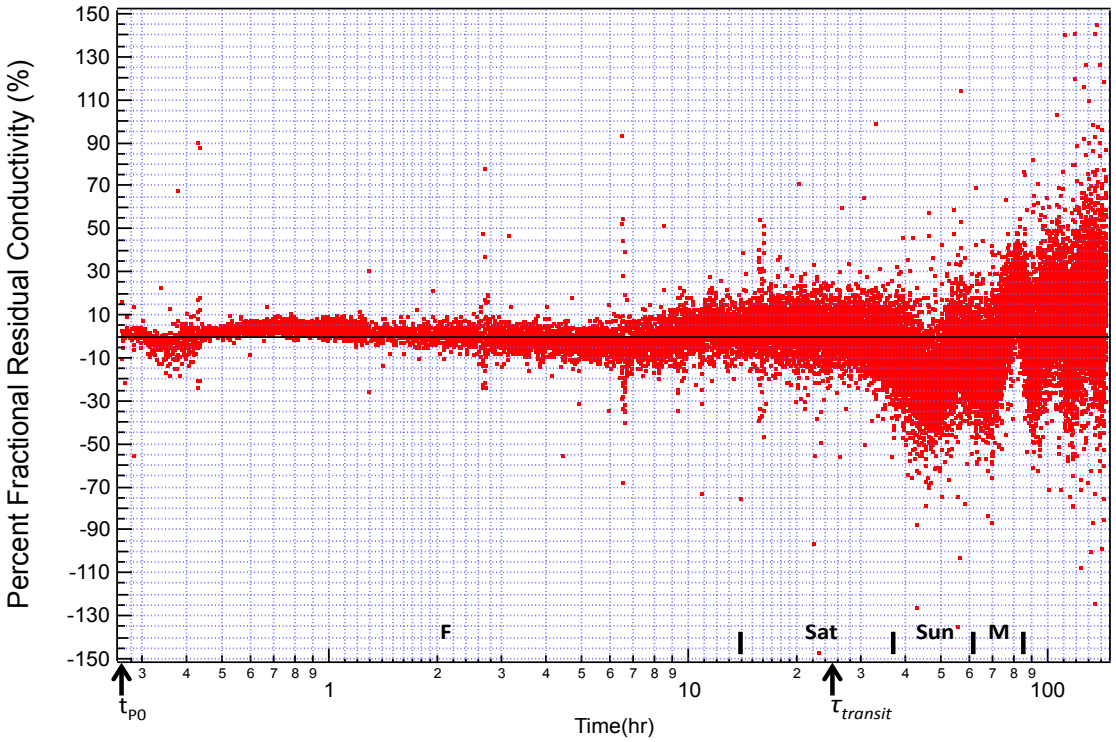

FIG 30. Percent fractional residual three-polarization radiated PI conductivity versus time: linear-log plot.

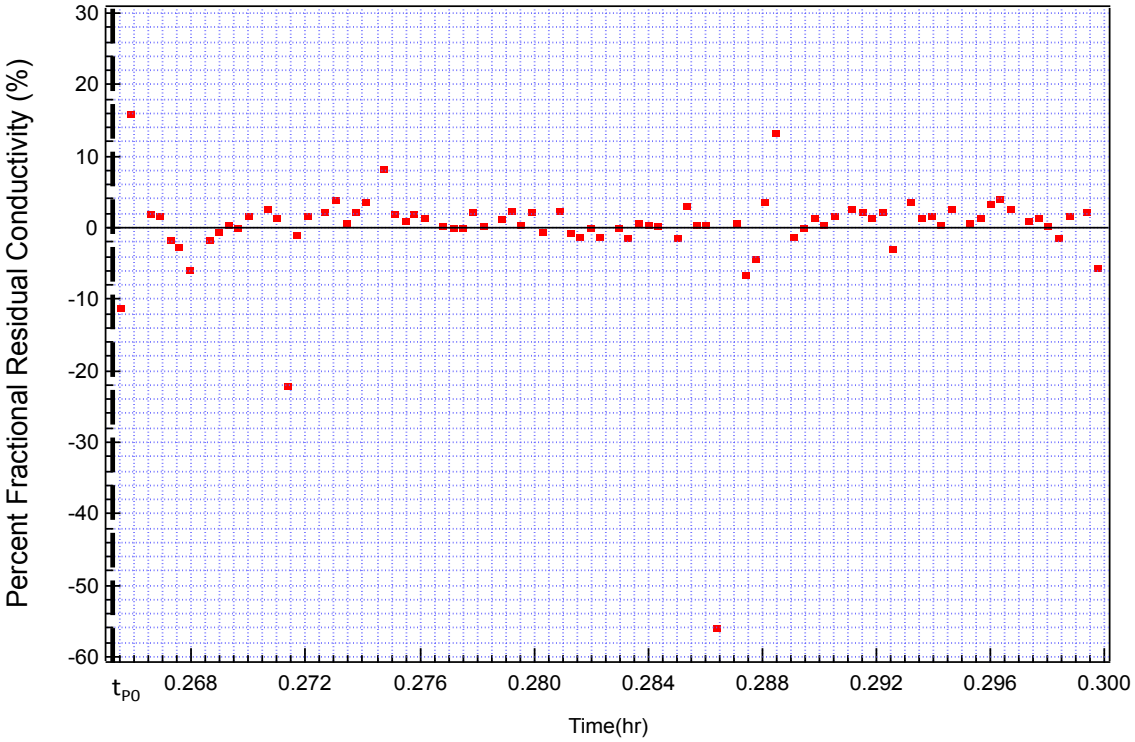

FIG 31. Percent fractional residual three-polarization radiated PI conductivity (polarization zoom) versus time: linear-linear plot.

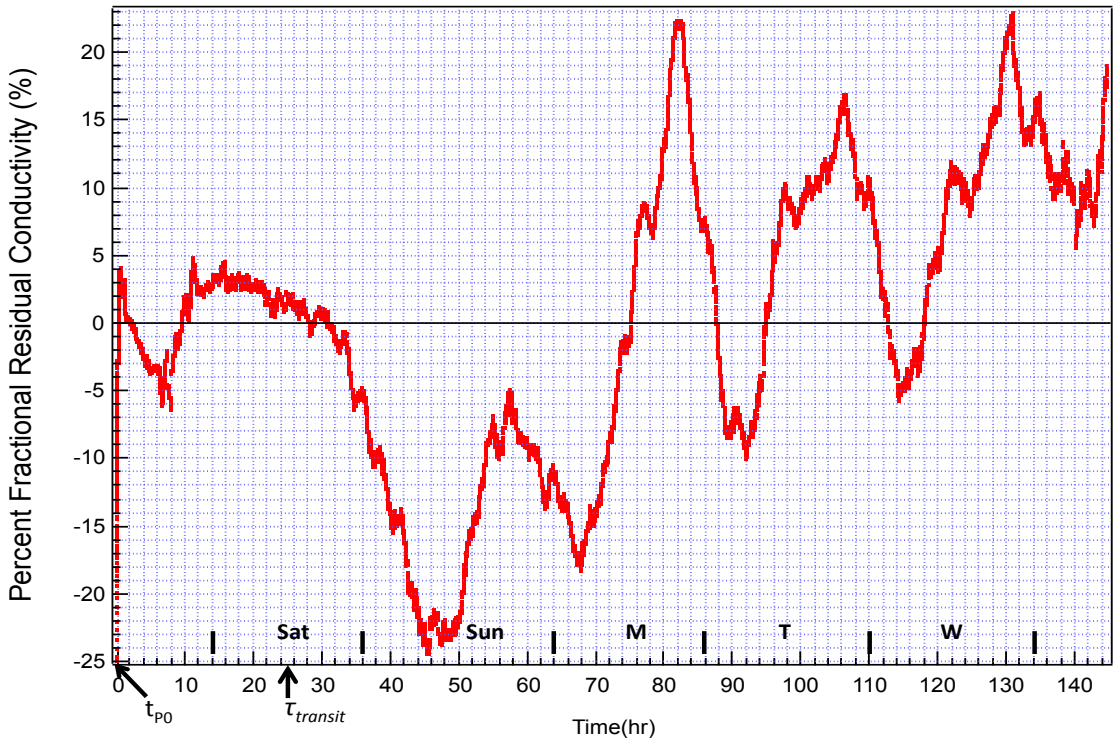

FIG 32. Percent fractional residual one-polarization smoothed radiated PI conductivity versus time: linear-linear plot.

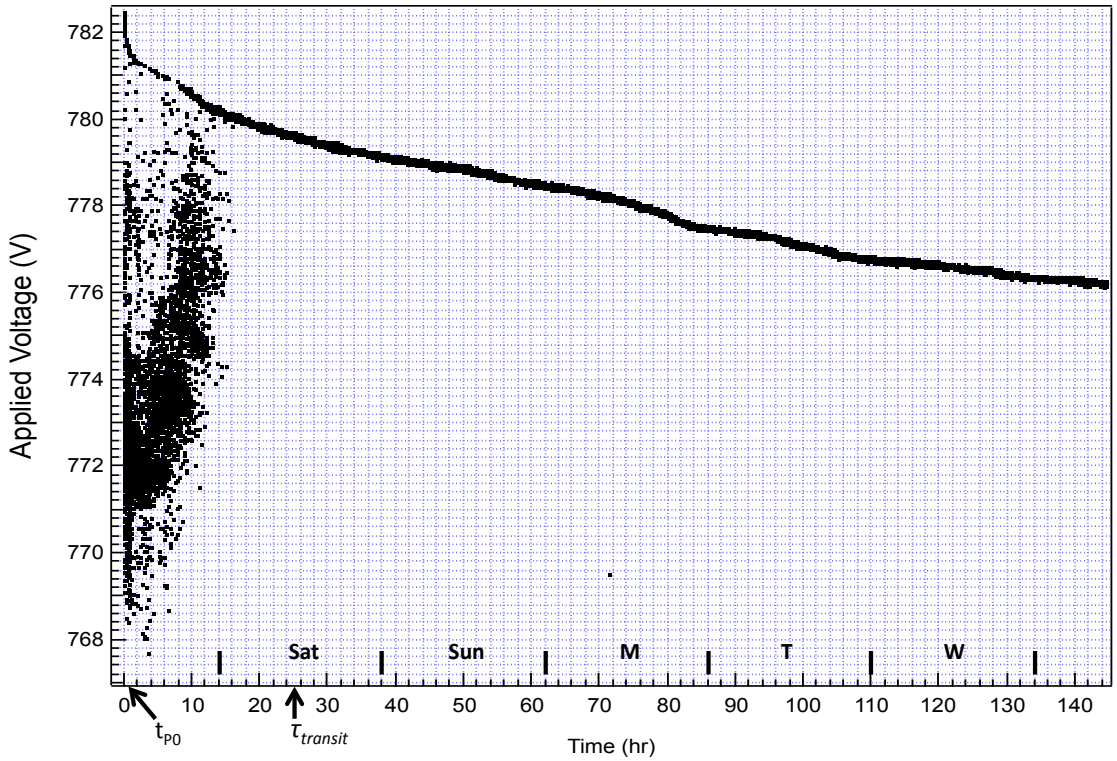

FIG 33. Radiated PI applied voltage versus time.

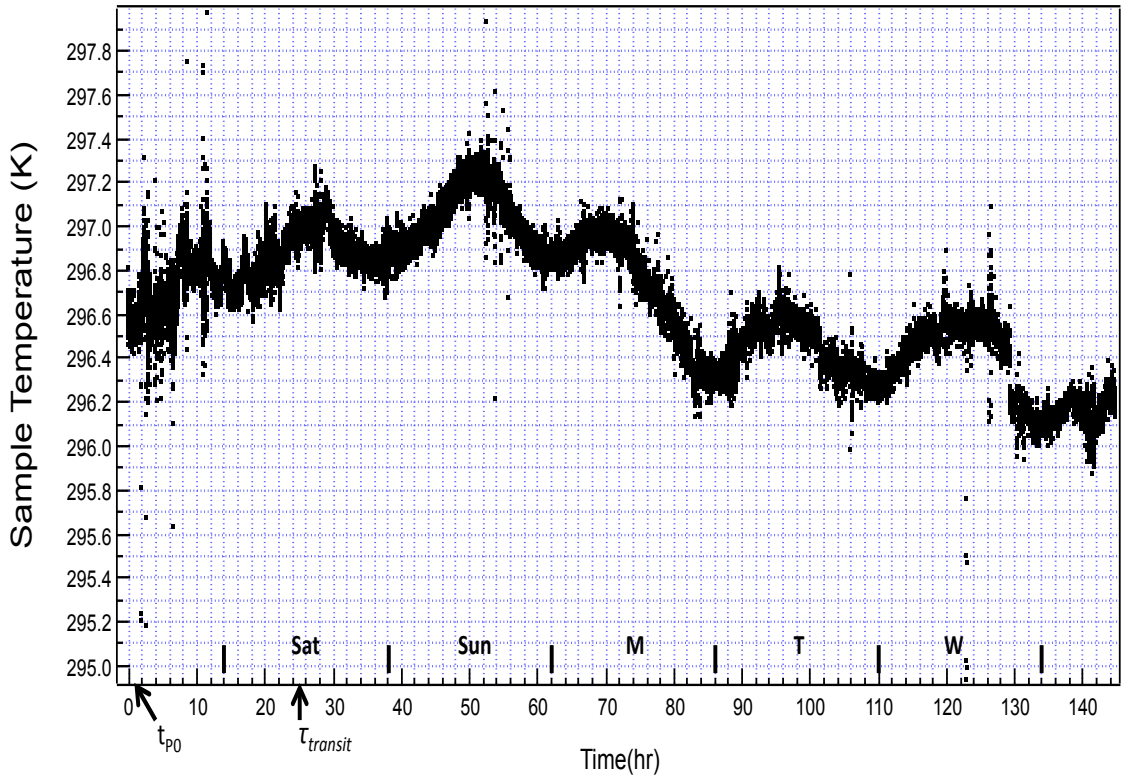

FIG 34. Radiated PI sample temperature versus time.

The radiated PI conductivity data were also fit using the three-polarization term model, (4). Figures 20, 21, and 25 are graphs of the radiated PI conductivity fit using (2) and Figures 22, 23, and 26 use (4). These also include the individual contributions of the constituent terms in (2) and (4). Figures 25 and 26 are log-linear plots of the polarization region of the conductivity data (approximately 0.26-0.3 hr). Figures 27 through 32 are plots of the percent fractional residual conductivity versus time using (3). The graph of applied voltage versus time for the radiated PI data set is shown in Figure 33 and Figure 34 is the sample temperature versus time. Figure 33 shows a linear drift in the voltage (due to battery discharge) of about 31 mV/hr after the initial period of instability, which is approximately the first 16 hr. This systematic effect due to linear voltage drift is canceled out in the conductivity calculation. Figure 24 shows the smoothed radiated PI conductivity and the percent fractional residual of the smoothed radiated PI conductivity is shown in Figure 32. The radiated PI conductivity data were averaged over 200 data points to generate Figure 24. Figure 27 is included for completeness to show how well all the data collected are fit by (2). The parameters resulting from fitting the radiated PI data with (2) and (4) are displayed in Table 2.

The radiated PI conductivity data is modeled well by (2) and (4), as shown in Figures 27-32. Even in the later part of the data, where fluctuations in temperature (Figure 33) appear to have caused fluctuations in the conductivity, the percent error, as shown in the percent fractional residual plot in Figure 28, is less than ±50% for the majority of data points. Again, the smoothed conductivity and its

percent fractional residual do not accurately represent the polarization region of the data. The accuracy in this area is shown in Figure 29, for the model fit with (2), and Figure 31, for the model fit using (4). Comparing Figures 29 and 31 clearly shows that three polarization terms fit this region with greater accuracy than only one polarization term: (2) has a maximum of -1000% error, with about half the points in this region having over -15% error (Figure 29). Figure 31 shows that the majority of points in the polarization region are fit to within ±4% by (4). As with the PI data, however, after the first 0.3 hr subsequent to when the voltage is applied, the two models are nearly identical (Figure 28 for (2) and Figure 30 for (4)). Additionally, Figure 32 shows that the majority of data points, given in the smoothed conductivity, are fit to within ±25% by (2). As with unirradiated PI, there appear to be two classes of agreement with the modeled conductivity: short and long-term variations. First, short-term variations (time scales on the order of minutes to hours) are small, on the order of 2-3%. Longer short-term variations are on the order of tens of hours and are larger, around ±5-20% (Figure 32). The long-term variation is shown in Figure 32 (see 45 hr to 140 hr), which is ±25%. The longer trend may be due to systematic errors such as temperature or current zero drifts, as with unirradiated PI.

Here, as with the fits of (2) and (4) for unirradiated PI, Figure 32 shows the areas where the models over-predict or under-predict the data because (2) and (4) are noticeably different only in the polarization region. From 30-75 hr the models under-predict the radiated PI data and from 120 hr to the end of data collection, the models over-predict the data. Also, Figure 29 shows that (2) again under-predicts the measured conductivity in the polarization region.

Figure 34 shows that, as with the unirradiated PI data, the sample temperature fluctuated on about 24 hr cycles, corresponding to daily fluctuations in room temperature.

C. LDPE

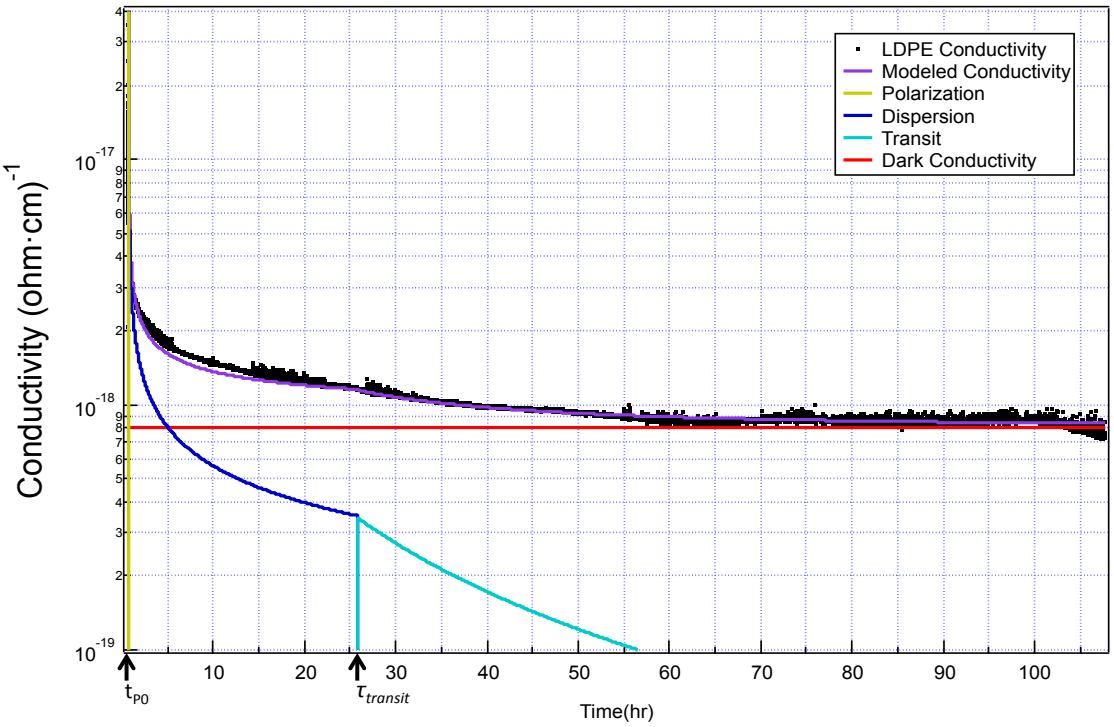

FIG 35. LDPE conductivity (polarization fit) versus time: log-linear plot.

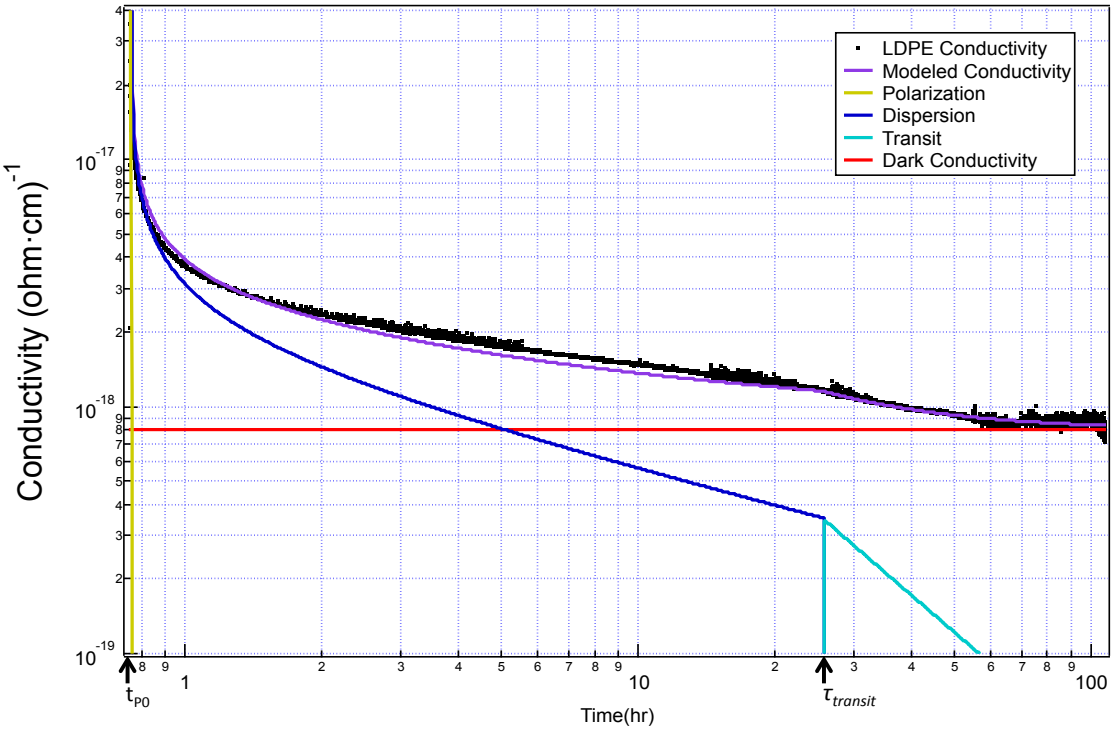

FIG 36. LDPE conductivity (polarization fit) versus time: log-log plot.

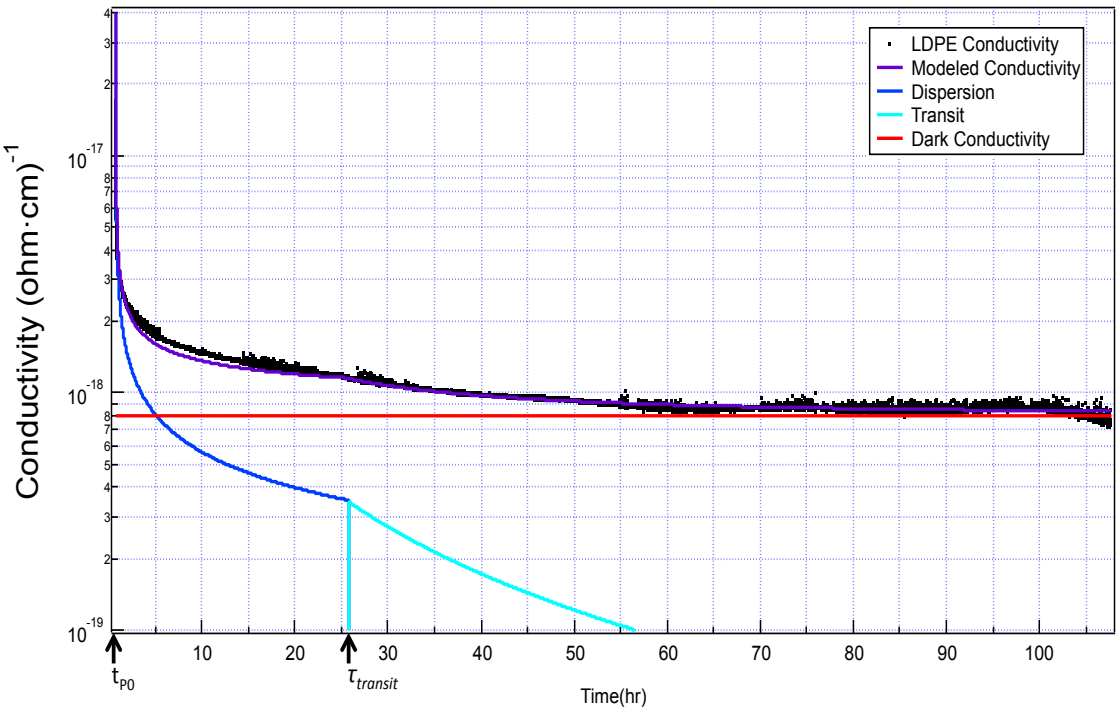

FIG 37. LDPE conductivity (no-polarization fit) versus time: log-linear plot.

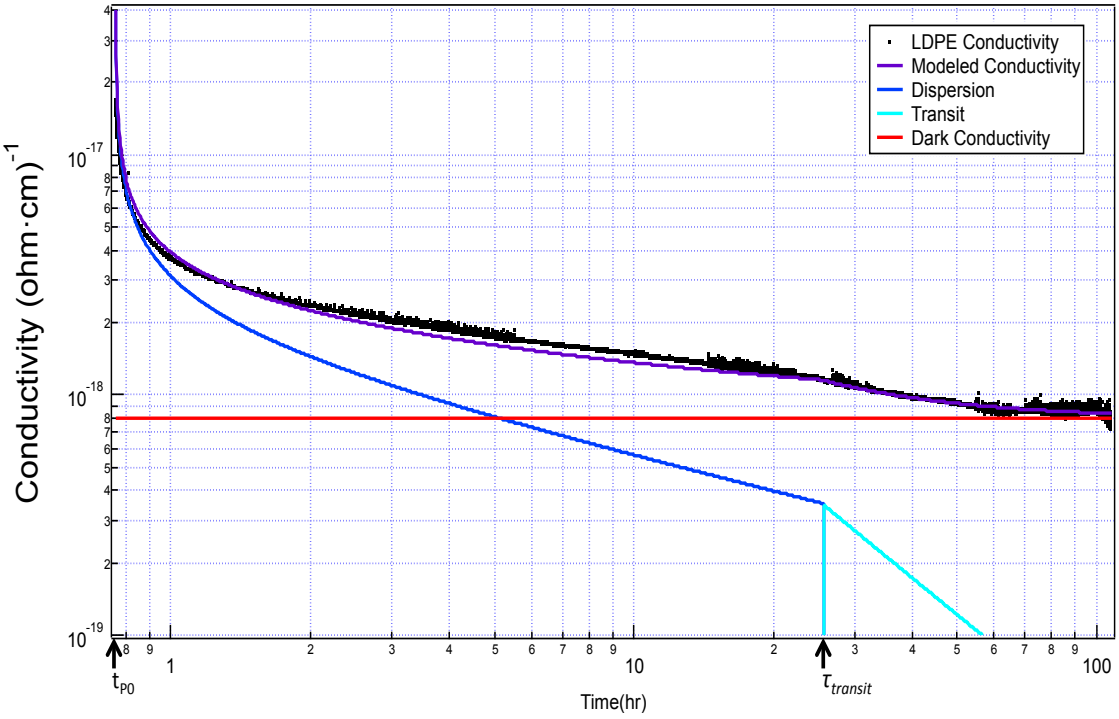

FIG 38. LDPE conductivity (no-polarization fit) versus time: log-log plot.

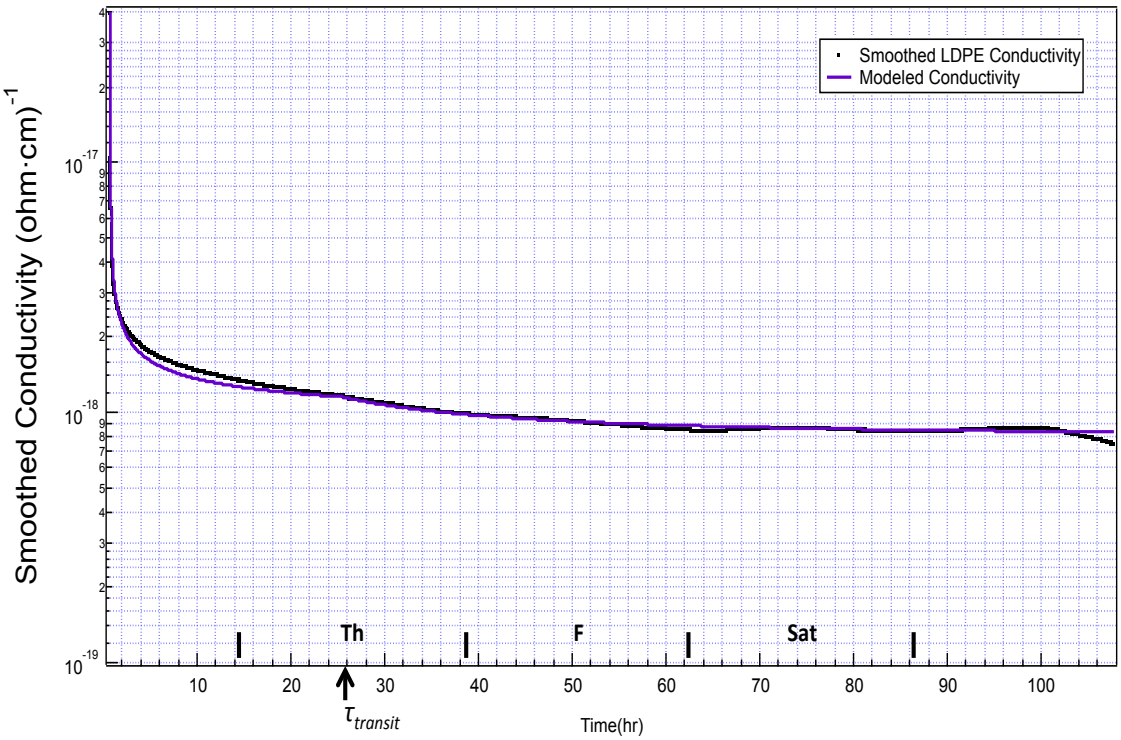

FIG 39. Smoothed LDPE conductivity (polarization fit) versus time: log-linear plot.

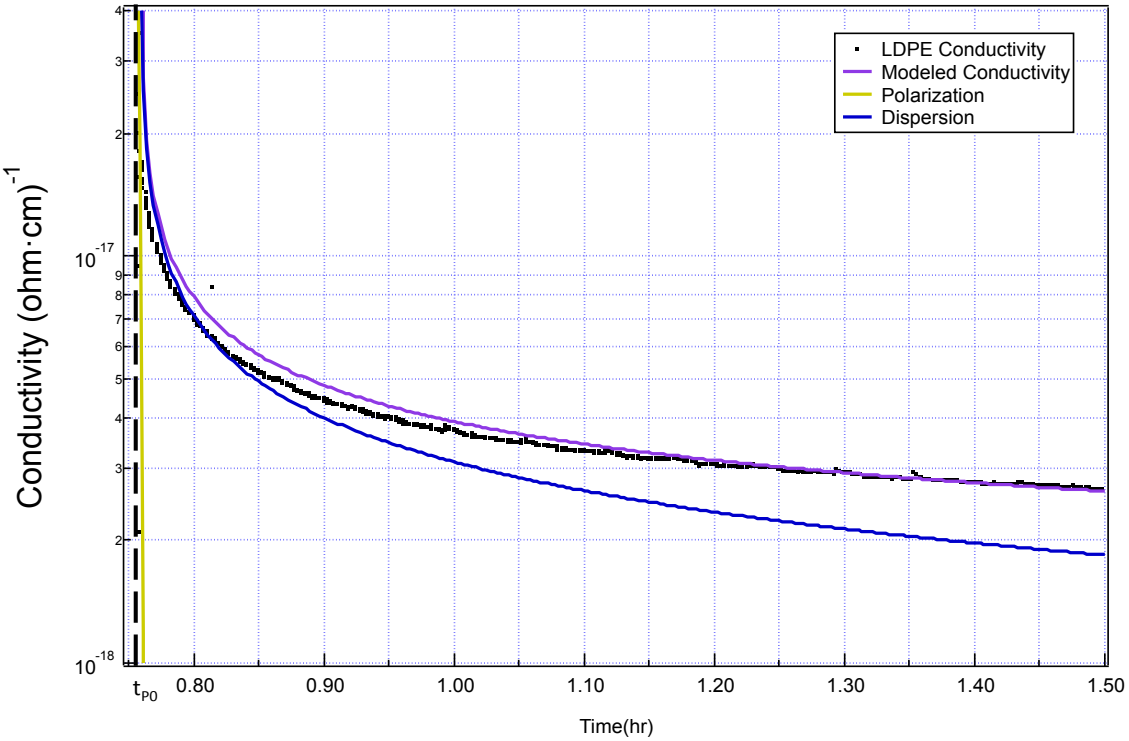

FIG 40. LDPE conductivity (polarization fit and polarization zoom) versus time: log-linear plot.

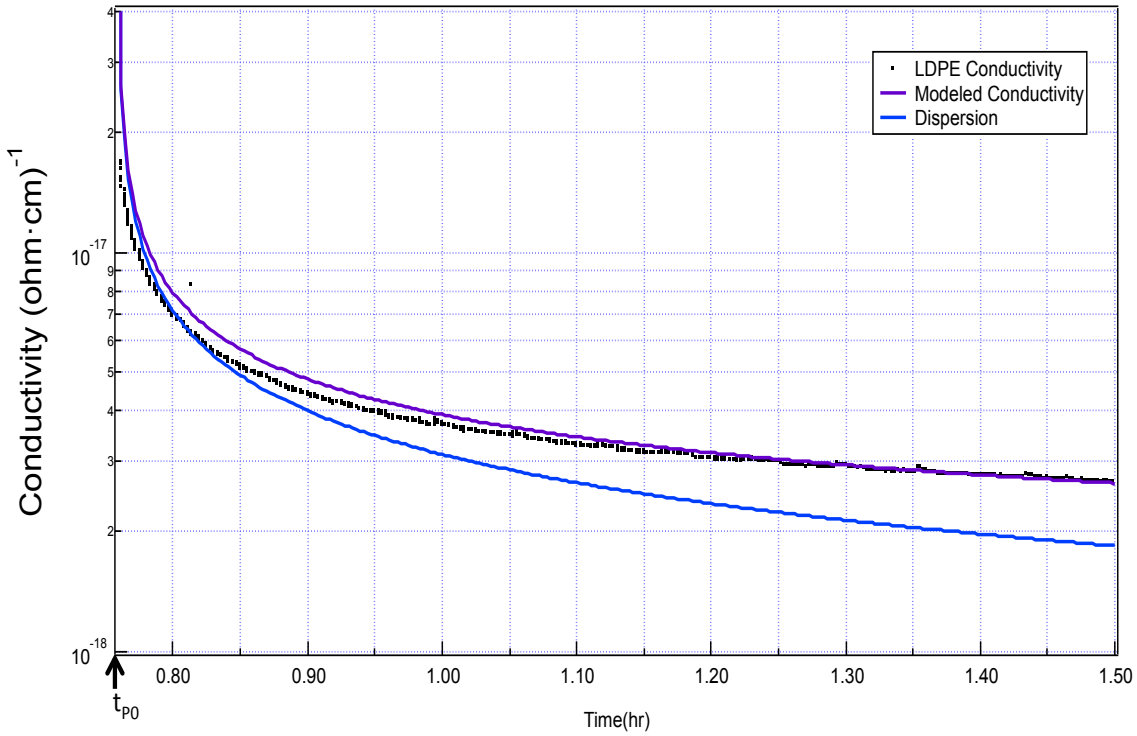

FIG 41. LDPE conductivity (no-polarization fit and polarization zoom) versus time: log-linear plot.

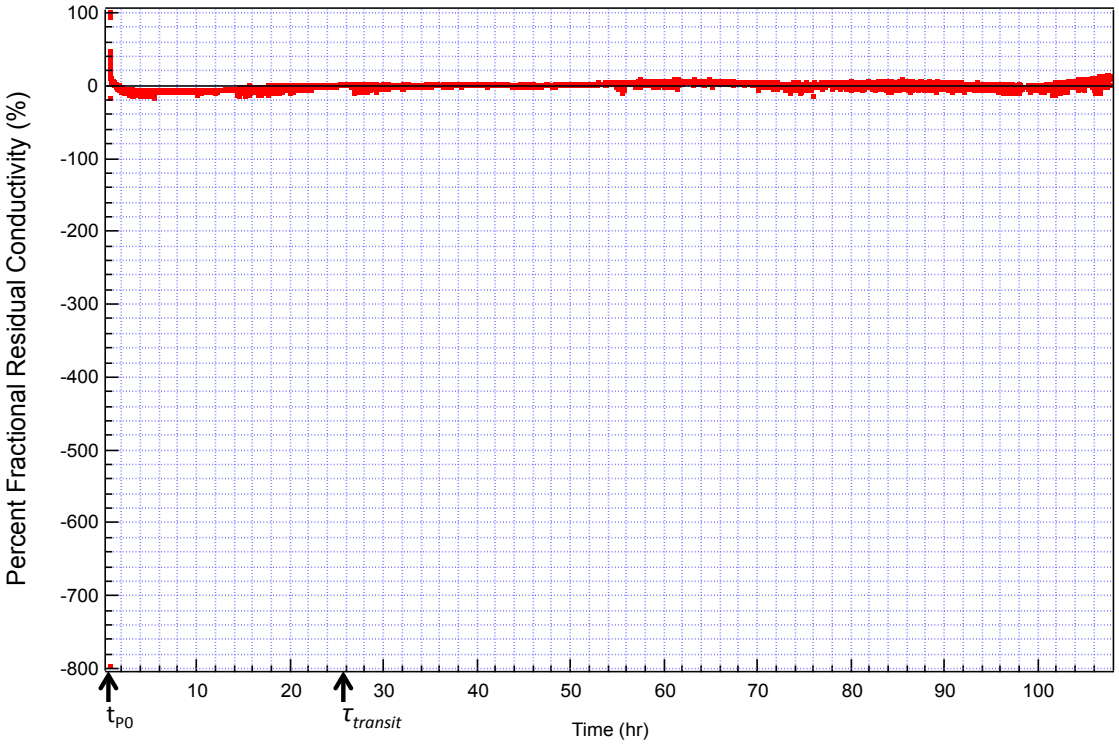

FIG 42. Percent fractional residual one-polarization LDPE conductivity versus time: linear-linear plot.

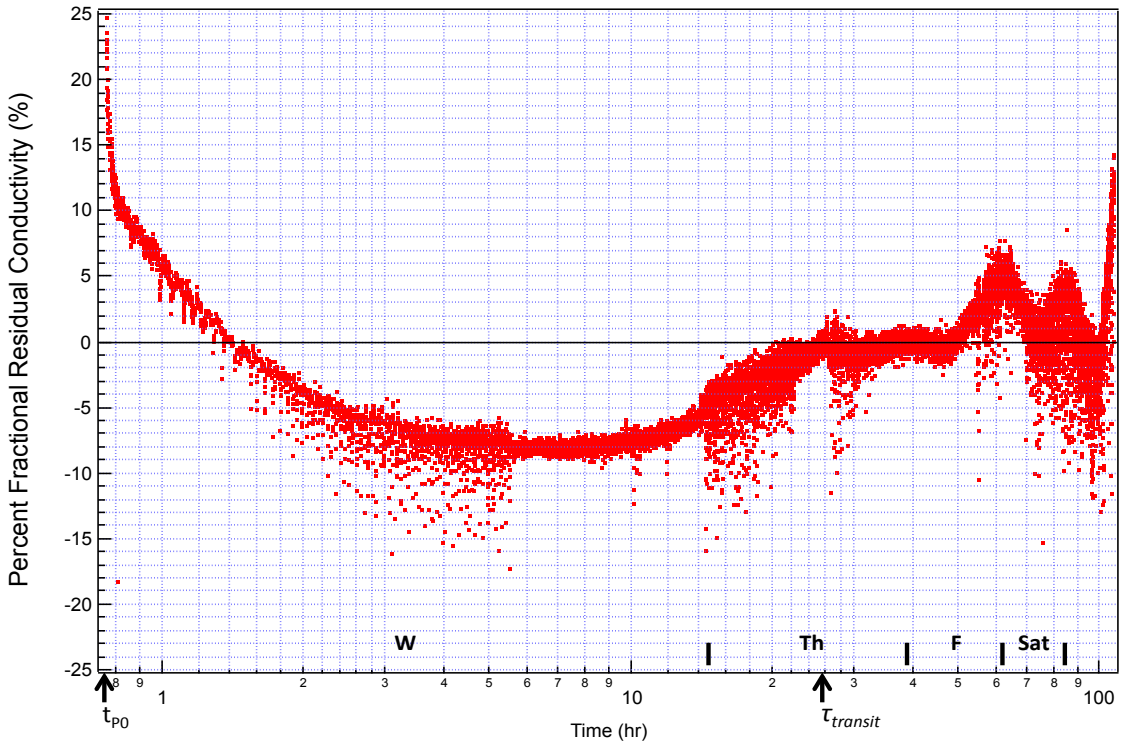

FIG 43. Percent fractional residual one-polarization LDPE conductivity versus time: linear-log plot.

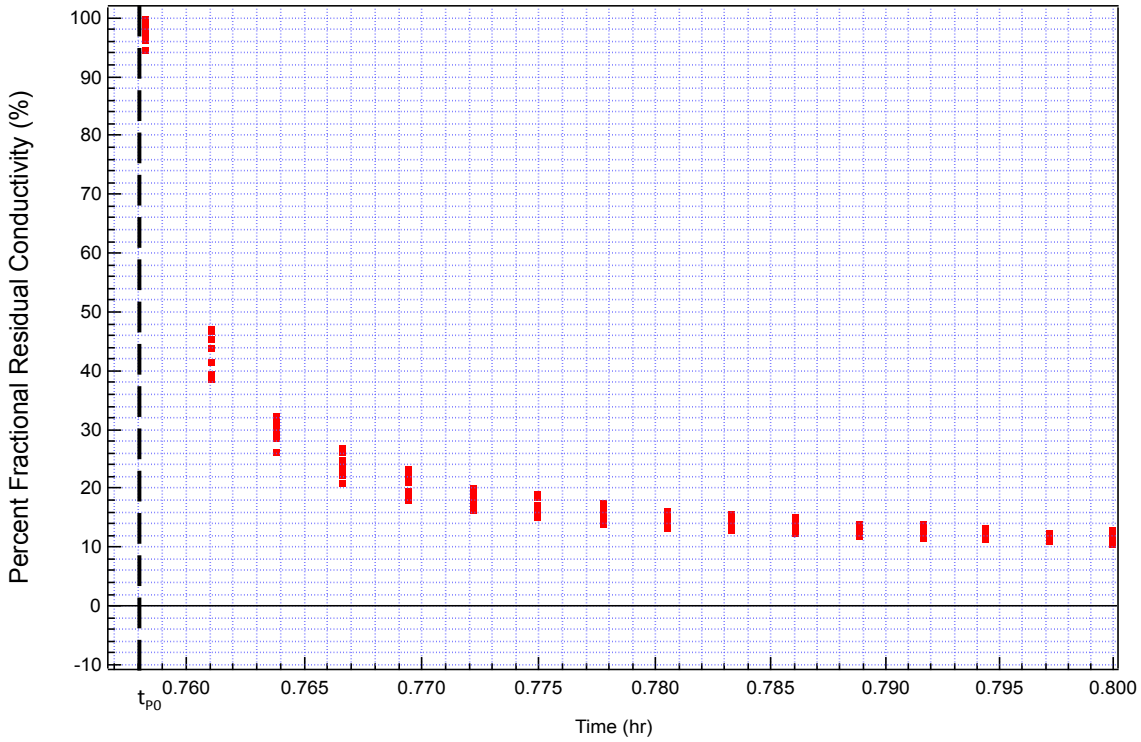

FIG 44. Percent fractional residual one-polarization LDPE conductivity (polarization zoom) versus time: linear-linear plot.

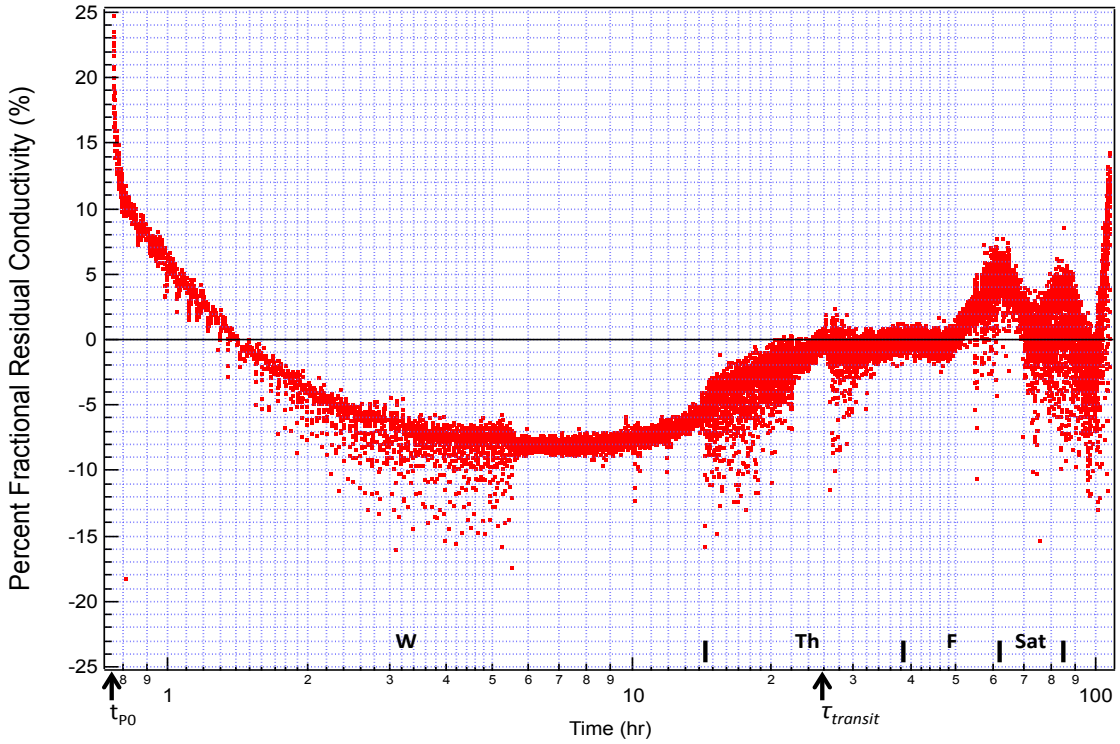

FIG 45. Percent fractional residual no-polarization LDPE conductivity versus time: linear-log plot.

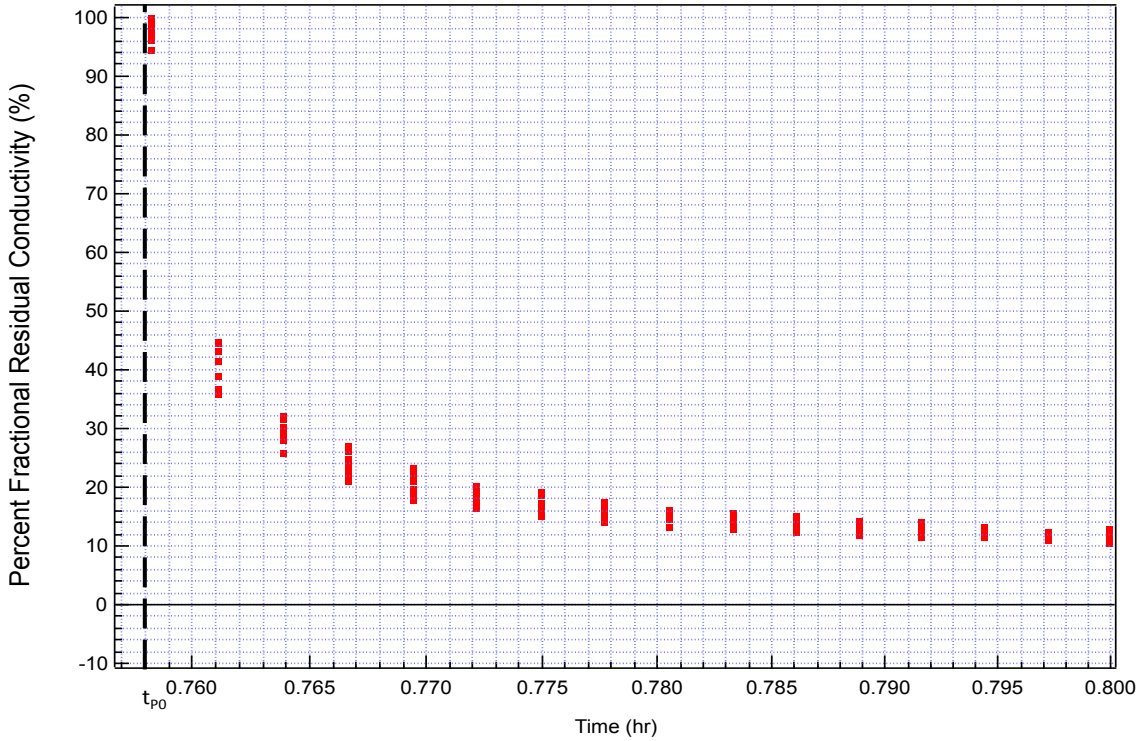

FIG 46. Percent fractional residual no-polarization LDPE conductivity (polarization zoom) versus time: linear-linear plot.

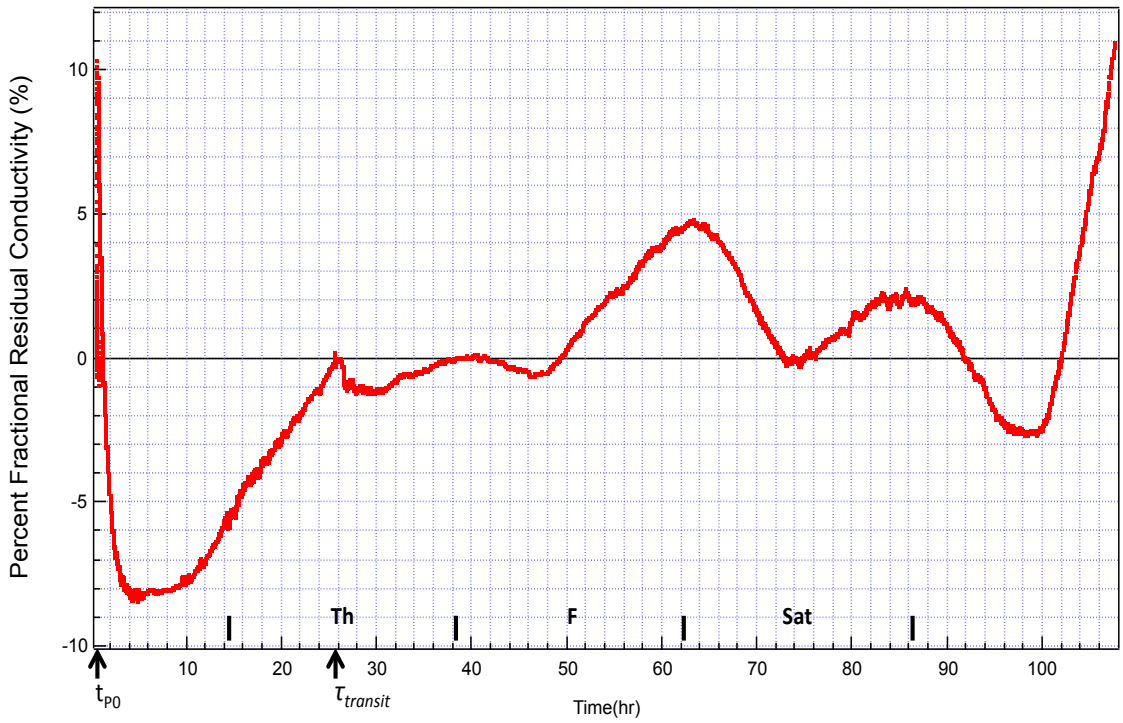

FIG 47. Percent fractional residual one-polarization smoothed LDPE conductivity versus time: linear-linear plot.

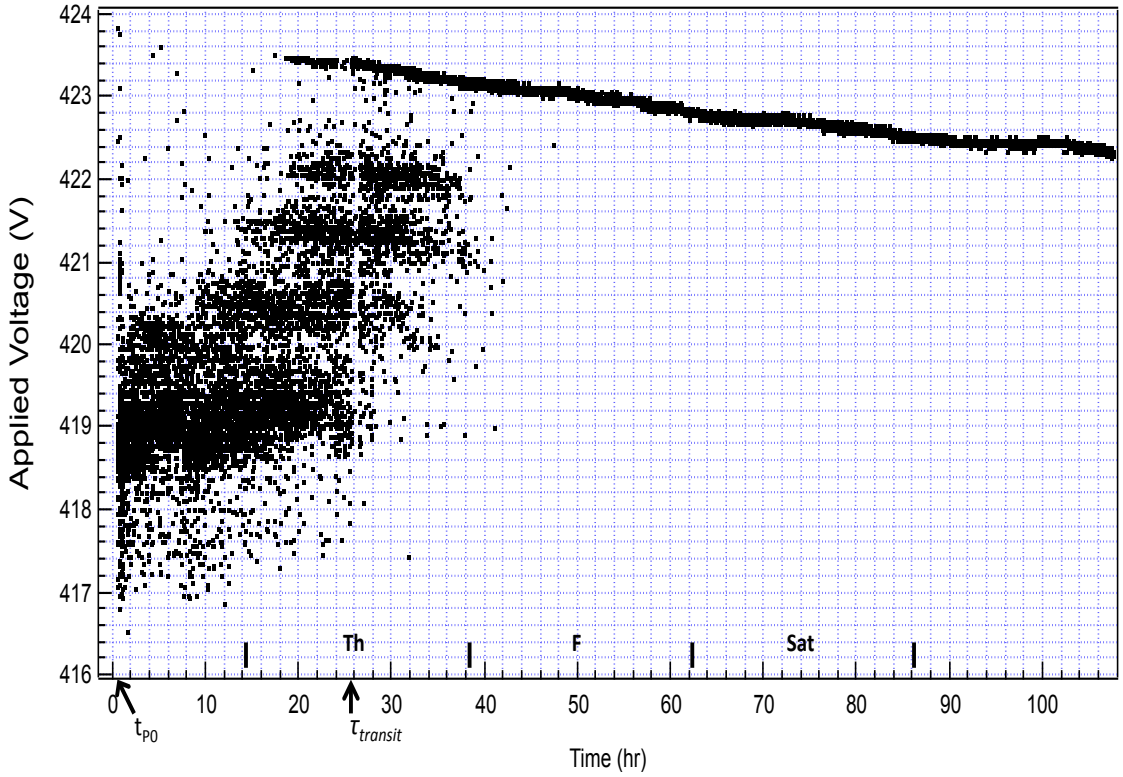

FIG 48. LDPE applied voltage versus time.

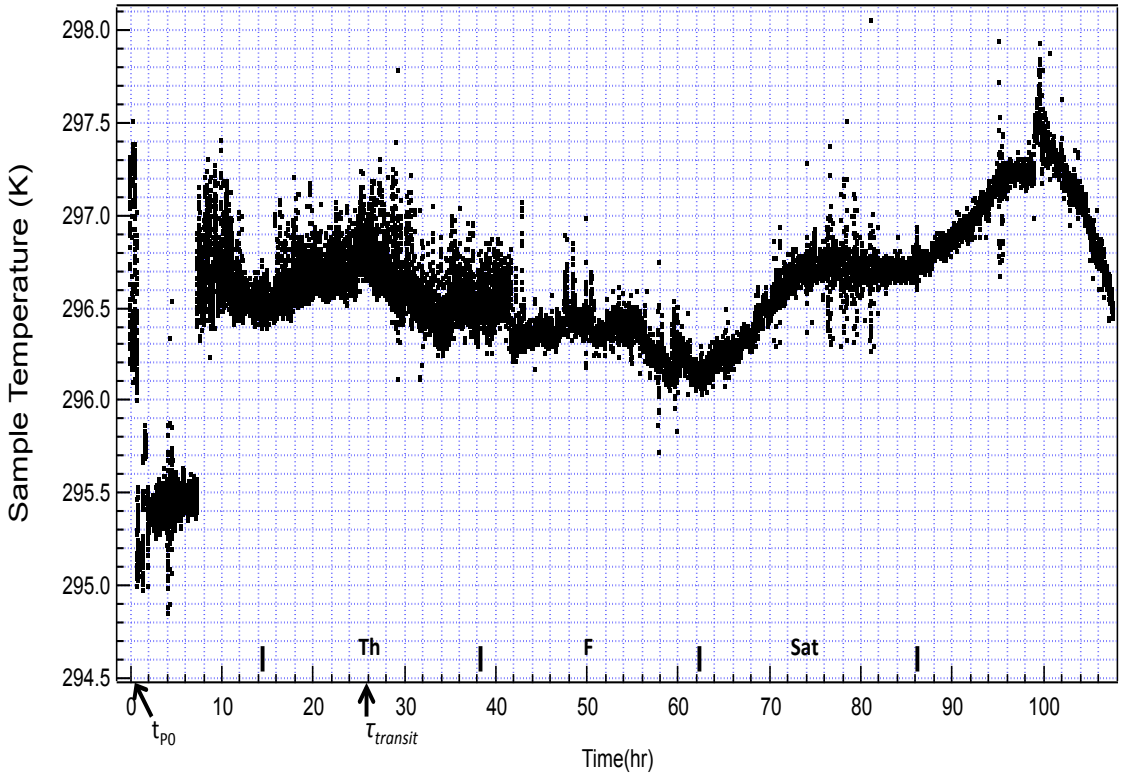

FIG 49. LDPE sample temperature versus time.

The conductivity models shown above for LDPE do not include a fit with the three-polarization model because it made the resulting model more inaccurate overall. Instead, fitting the LDPE data using a model without any polarization terms was attempted:

$$\sigma_{total}(t) = \sigma_{Sat} + \sigma^0_{diff}t^{-1} + \sigma^0_{disp}t^{-(1-\alpha)}\Theta(\tau_{trans} - t) + \sigma^0_{trans}t^{-(1+\alpha)}\Theta(t - \tau_{trans}) \quad (5)$$

Figures 35 through 41 are graphs of LDPE conductivity versus time. They include the modeled conductivity fit using (2) and (5) for one-polarization (Figures 35, 36, and 40) and no-polarization (Figures 37, 38, and 41) term fits, and the individual contributions of the constituent terms in (2) and (5). Figures 40 and 41 are log-linear plots of the polarization region (approximately 0.76-0.8 hr) of the conductivity data. Figures 42 through 47 are plots of the percent fractional residual conductivity versus time using (3). The smoothed LDPE conductivity is plotted in Figure 39 and its corresponding percent fractional residual plot is Figure 47. For Figure 39, the conductivity data were averaged over 100 data points. Figure 48 is a graph of the applied voltage for the LDPE data set, which shows a linear drift in the voltage (due to battery discharge) of roughly 12 mV/hr after the first 40 hr where the applied voltage was unstable. The systematic effect from this linear voltage drift is canceled out in the conductivity calculation. Figure 49 is a plot of sample temperature versus time to show how temperature variation may have affected the LDPE conductivity data. Figure 42 is included for completeness to show how well all

the data collected are fit by (2). The parameters resulting from fitting the LDPE data with (2) and (5) are displayed in Table 2.

The model of (2) does not fit the LDPE data as well in the region from 1.5 hr to 20 hr (Figures 43). This is believed to be due to temperature variations in the CVC chamber (Figure 49). The recorded temperature in that region was highly erratic and displayed jumps of 2.5 K in about one second, which did not correlate to temperature variations in the room (more accurately depicted by Figure 34 in the region after about 42 hr based on the room temperature conjectured from the experience of the experimenters). The region from when the voltage was turned on (t_{p0}) to 25 hr had a standard deviation in temperature of 0.6 K and the region from 25 hr to the end of the data run had a standard deviation of 0.3 K. So, the region in question had double the standard deviation of the less noisy period. Thus, the temperature data in these areas may have been erroneously recorded by the data measurement system, yielding inaccurate data there. Because of that, it was not possible to determine if temperature fluctuations could have caused variations making the models not fit the data well in that region. However, as shown in Figures 43 and 45, (2) and (5) fit the LDPE conductivity data even better than (2) and (4) fit the unirradiated PI and radiated PI data.

As shown in Figures 43 and 45, the majority of the LDPE data is fit to within ±15% by both (2) and (5) and the models of (2) and (5) are nearly identical in fitting the LDPE data. Figure 47, based on the smoothed LDPE conductivity, shows that the majority of data points are fit to within ±10% by (2). The accuracy of (2) and (5) in the polarization part of the data is shown in Figures 44 and 46 because the smoothed conductivity is not accurate in that area. Upon examination, Figures 44 and 46 show that there is virtually no difference for this LDPE data between (2) and (5) in the polarization region as well. In fact, as shown in Figures 44 and 46, looking at the time between 0.76 hr and 0.78 hr, the data is fit slightly better by (5) than by (2). Other than that, there is no noticeable difference between the two models. Thus, the polarization term has no significant contribution to the model of conductivity for this LDPE data. Here, as with unirradiated and radiated PI, there appear to be two classes of agreement with the modeled conductivity. Short-term variations occur on two time scales: on the order of minutes to hours and on the order of tens of hours. For the scale of minutes to hours, variations are on the order of 1% (Figure 47). For time scales on the order of tens of hours, variations are on the order ±1-14% (Figure 47). Figure 47 also shows a long-term trend (see 10 hr to 102 hr) that is ±6%. The longer trend may be due to systematic errors such as temperature or current zero drifts, as is hypothesized with unirradiated and radiated PI. The sharp decrease in conductivity from 100-107 hr is believed to be due to temperature effects (Figures 39 and 49).

Figure 47 shows the accuracy of both (2) and (5), when not considering the polarization area of the data. It is seen from this that (2) and (5) over-predict the LDPE conductivity data in a couple regions (50-72 hr and 76-92 hr) and under-predict in the region of 1.5-20 hr mentioned previously. Figures 44 and 46 show that both fits over-predict the LDPE data in the polarization region. This is because the dispersive term dominates there and over-predicts the data (Figure 41). Using

values for α_{disp} and σ_{disp}^{0} that better fit the region from 1.5-10 hr was attempted. This resulted in a fit using (5) that under-predicted in the polarization region, which allowed for altering the modeled conductivity using (2) and also attempting to use a three-polarization fit with (4). However, this change in the dispersive term resulted in disagreement of up to 20% between the modeled conductivity, for both (2) and (4), in the region of 10-25.8 hr. The change in values for the dispersive term also produced a value for α_{disp} that did not agree within error with the value for α_{trans}. Therefore, while this change did produce an improved accuracy in the polarization region for models using (2) and (4), it decreased the accuracy of modeled conductivity, for both (2) and (4), in the region from 10 hours to $\tau_{transit}$ by up to 20%. For those reasons, it was decided that the values given for the dispersive terms in Table 1 should be the ones used in this experiment because they produced the most accurate overall modeled conductivity.

III. Discussion and Conclusions

Figures 13, 28, and 43 show the model of conductivity in (2) fits all three data sets well. This can be seen by inspection of these percent fractional residual plots. Also, using the smoothed conductivity and Figures 17, 32, and 47, it is apparent that (2) is a very accurate model of conductivity for these materials. However, Figures 14, 29, and 44 show that (2) does not fit the conductivity well in the polarization region of the data. The three-polarization model of (4) increases the accuracy of the modeled conductivity in unirradiated PI and radiated PI to ≤±2% for unirradiated PI (Figure 16) and ≤±3% for radiated PI (Figure 31) in the polarization region of the conductivity data. But, LDPE is fit just as well by (5), without any polarization, as by (2) (see Figures 44 and 46). This implies that the polarization processes taking place differ based on material. Furthermore, in [8], it is stated that, though LDPE has a non-polar structure, fast polarization times are evident in its measured conductivity using the CVC method. This study would suggest that the initial curve, or the polarization region of the measured conductivity (Figure 40) does not have a steep curve due to a polarization mechanism. This is suggested by Figures 44 and 46, which indicate negligible contributions due to any polarization term in the modeled conductivity. However, this cannot be said conclusively because other attempts were made at fitting the LDPE conductivity data that did include polarization terms. These were accurate to within ±10% in the polarization region, but decreased the accuracy by up to 20% in the interval between 10 hr and 25.8 hr ($\tau_{transit}$). To determine the specific polarization processes, or lack thereof, will require additional experimentation and research.

As shown in Figures 43 and 45, neither (2) nor (5) fit the LDPE data as well in the 1.5 hr to 20 hr region. But this is believed to due to temperature fluctuations in the CVC chamber and the temperature dependence of the sample. Temperature fluctuations also appear to have affected the conductivity of radiated PI (Figures 24 and 34). The decreased accuracy of the models in (2) and (4) during this region of fluctuating temperature can be seen in Figure 32. The changes in conductivity due to

changes in temperature were investigated further using the smoothed conductivity of unirradiated PI, radiated PI, and LDPE. Because the change in thickness and area should be negligible for the changes in temperature concerned (usually not more than 1.5 K) and because such changes should cancel each other in (1), it is believed that the changes in conductivity due to temperature must arise from changes in the applied voltage or the resulting current. To determine how temperature was causing the change in conductivity, graphs of current and voltage were compared to temperature graphs in regions of largest temperature fluctuations.

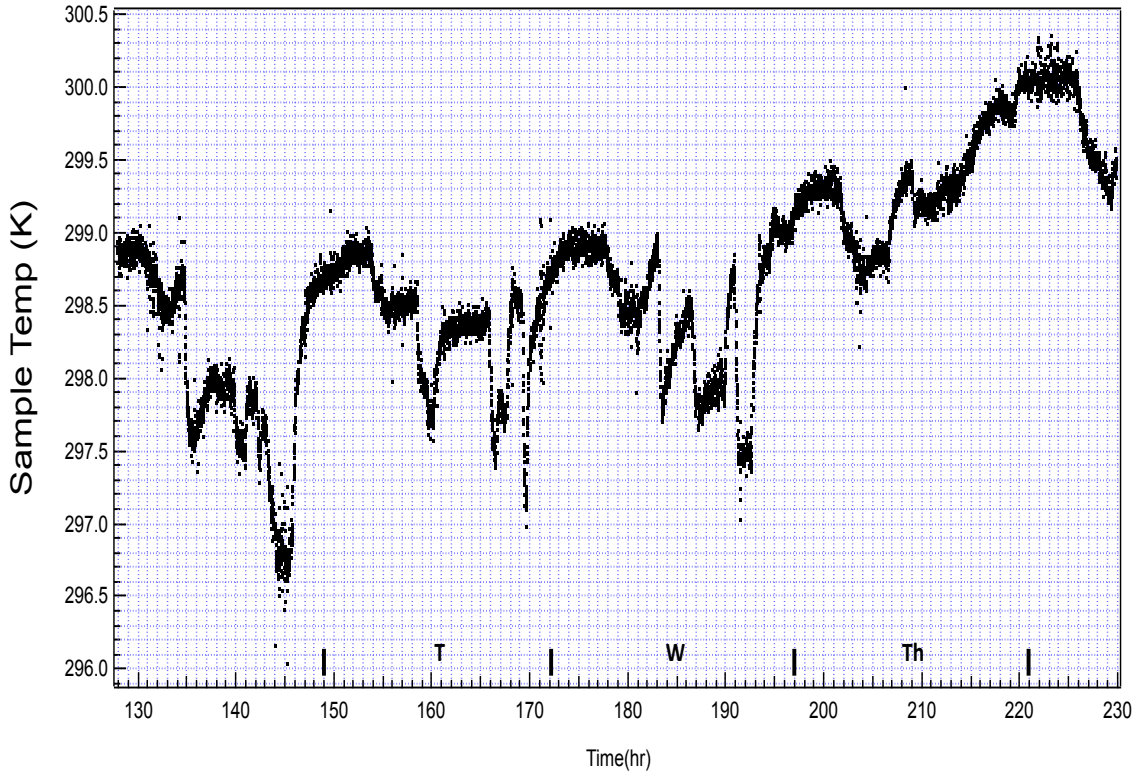

FIG 50. Unirradiated PI sample temperature versus time.

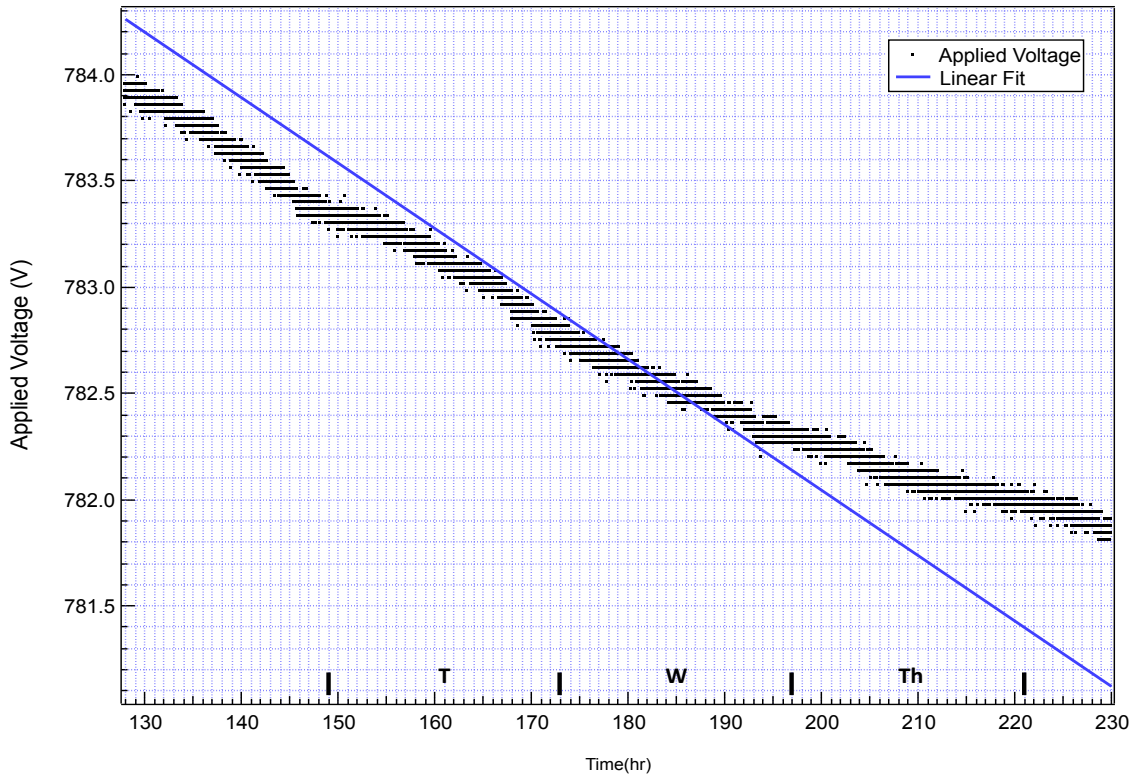

FIG 51. Unirradiated PI applied voltage versus time.

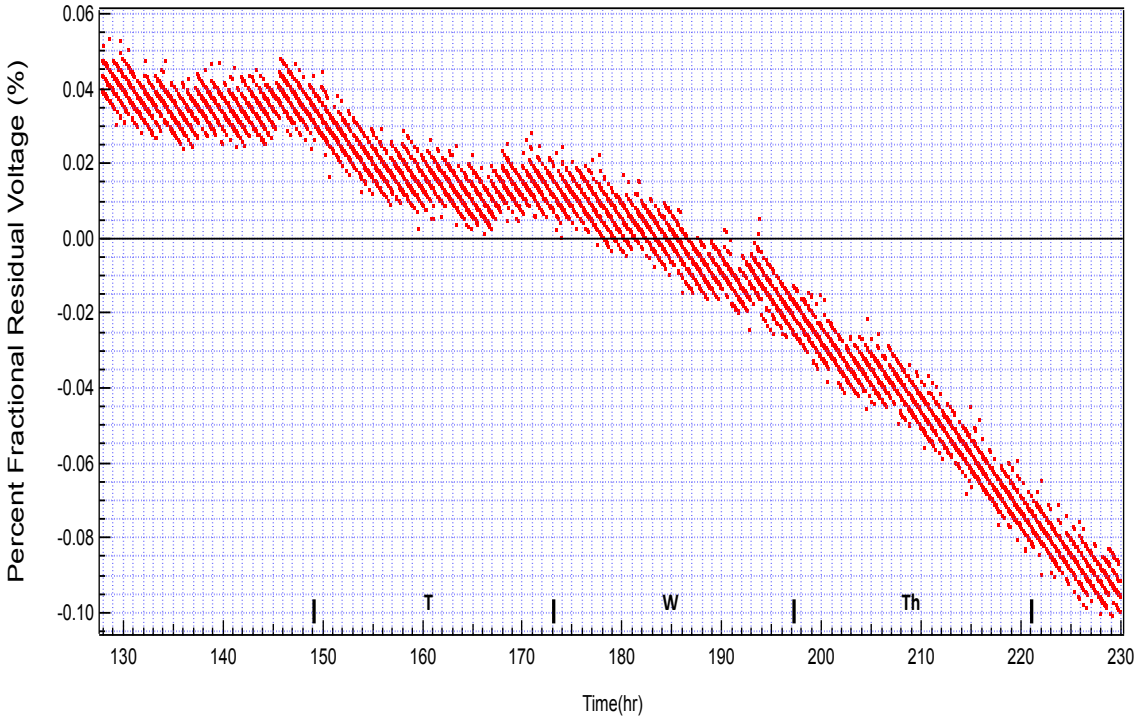

FIG 52. Percent fractional residual linear fit unirradiated PI applied voltage versus time: linear-linear plot.

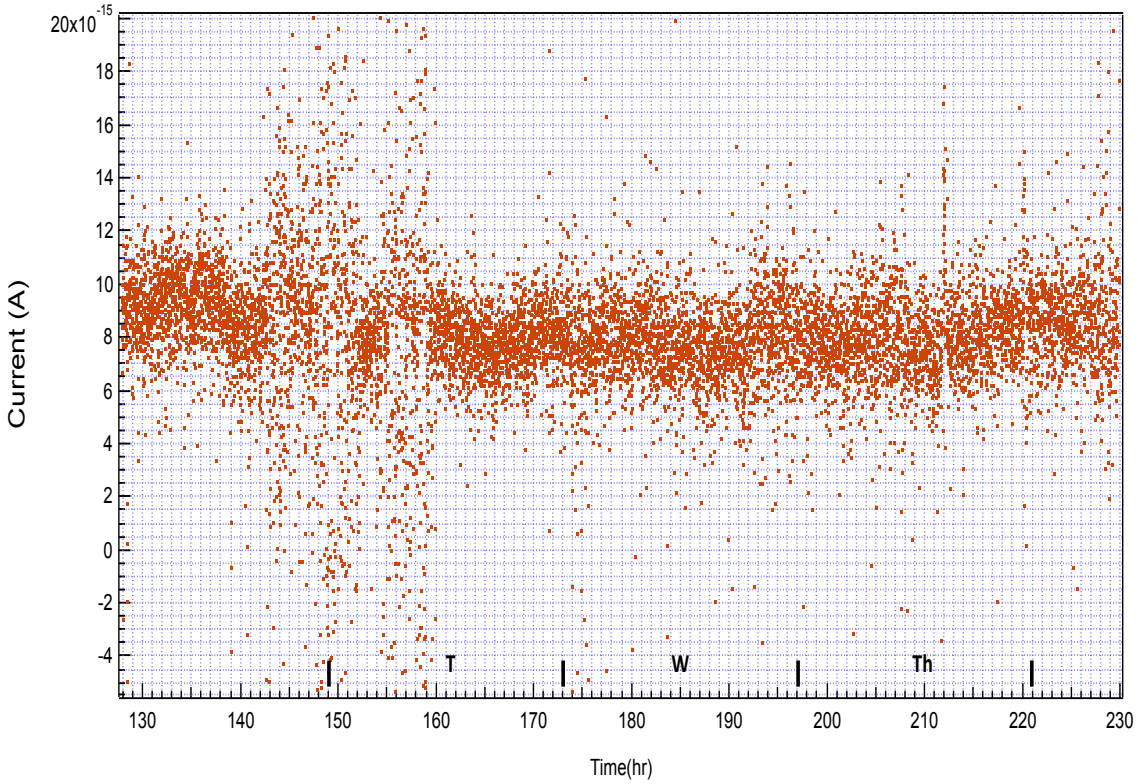

FIG 53. Unirradiated PI current versus time.

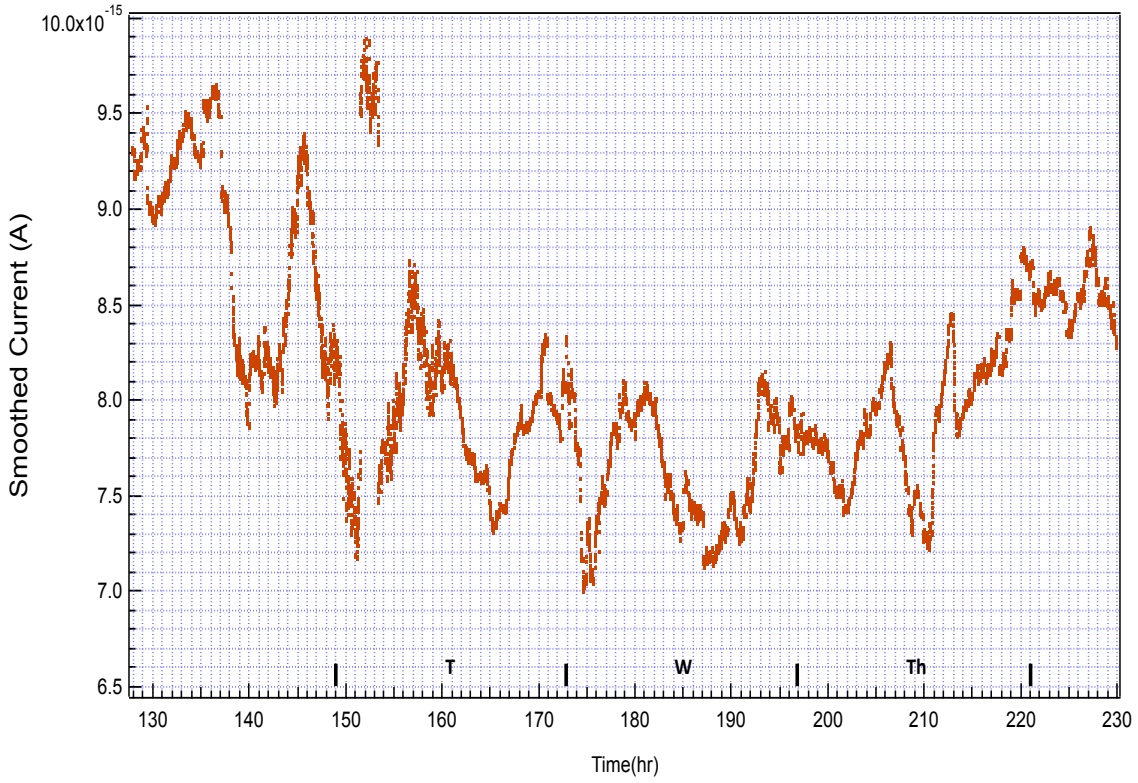

FIG 54. Smoothed unirradiated PI current versus time.

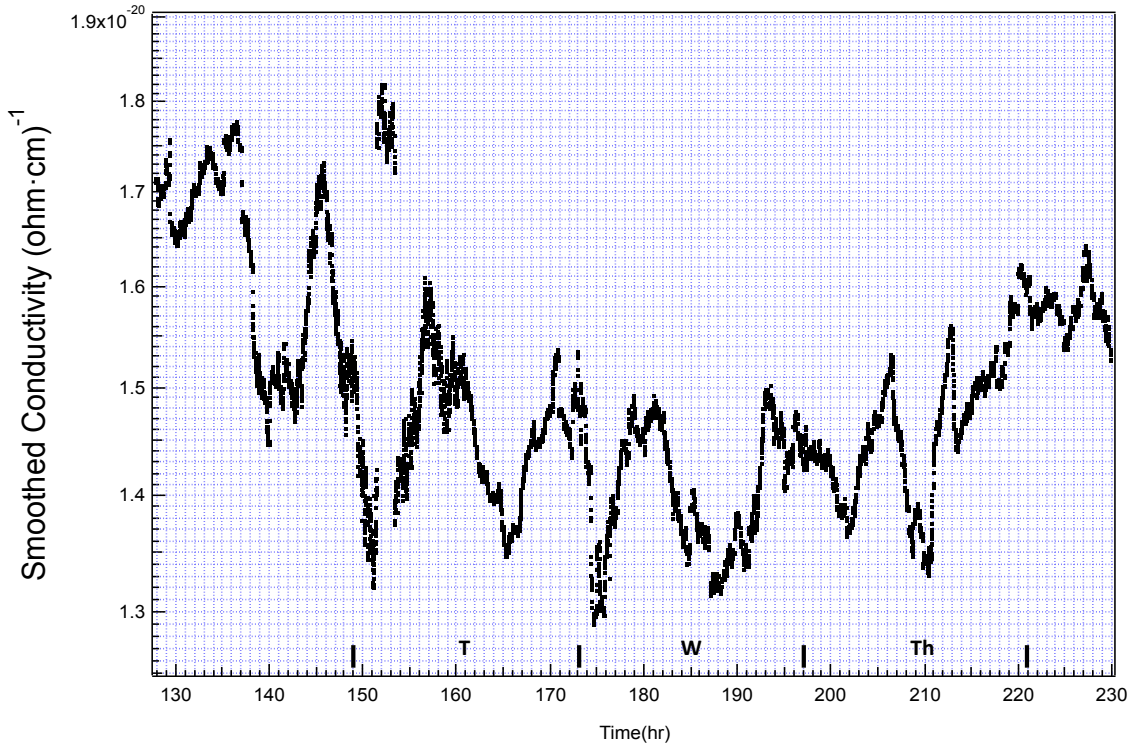

FIG 55. Smoothed unirradiated PI conductivity versus time: linear-linear plot.

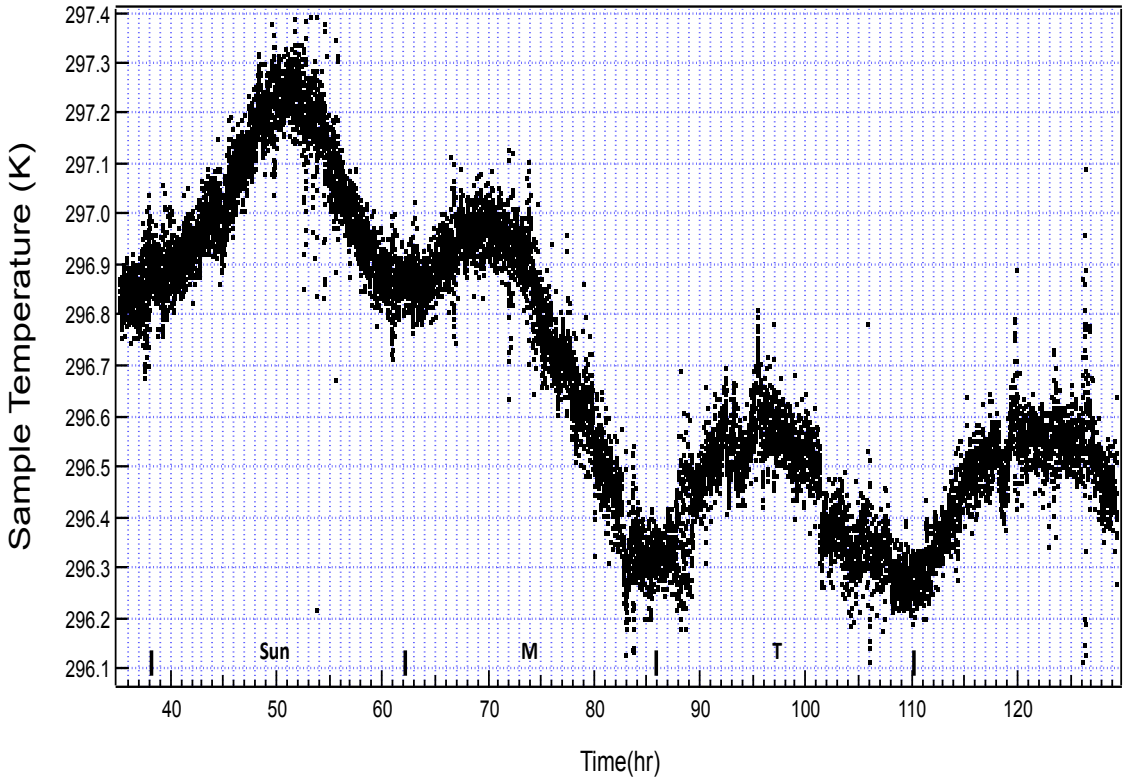

FIG 56. Radiated PI sample temperature versus time.

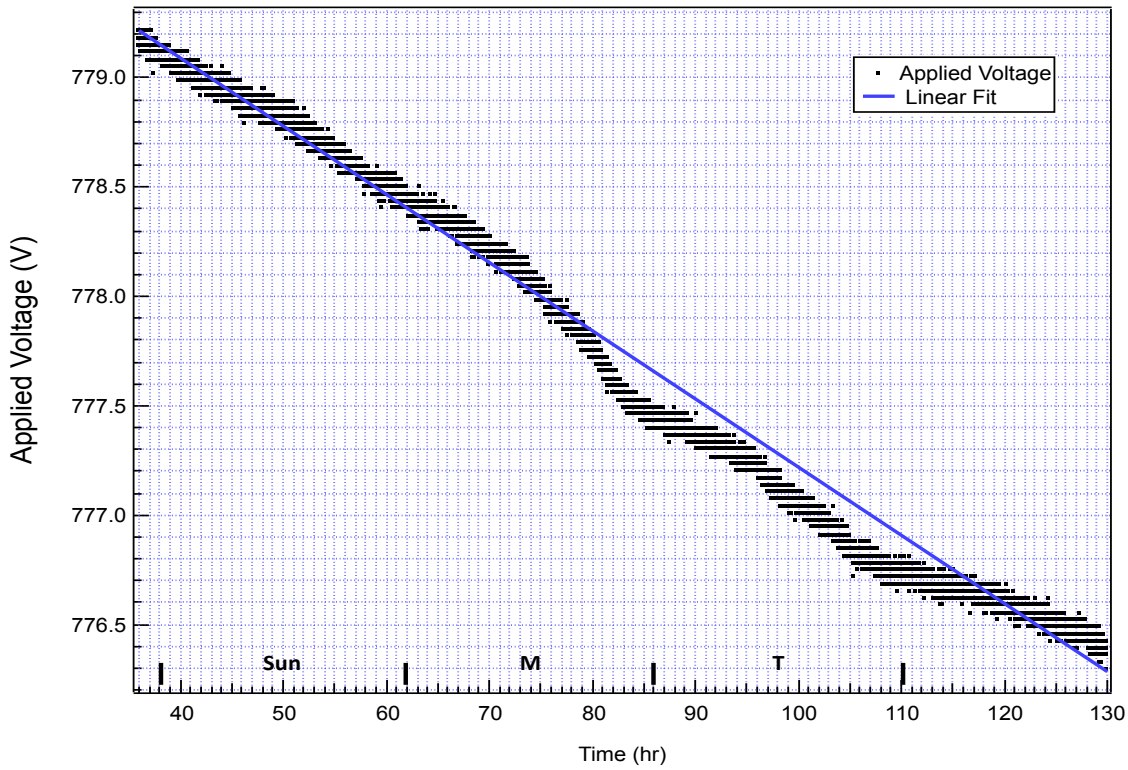

FIG 57. Radiated PI applied voltage versus time.

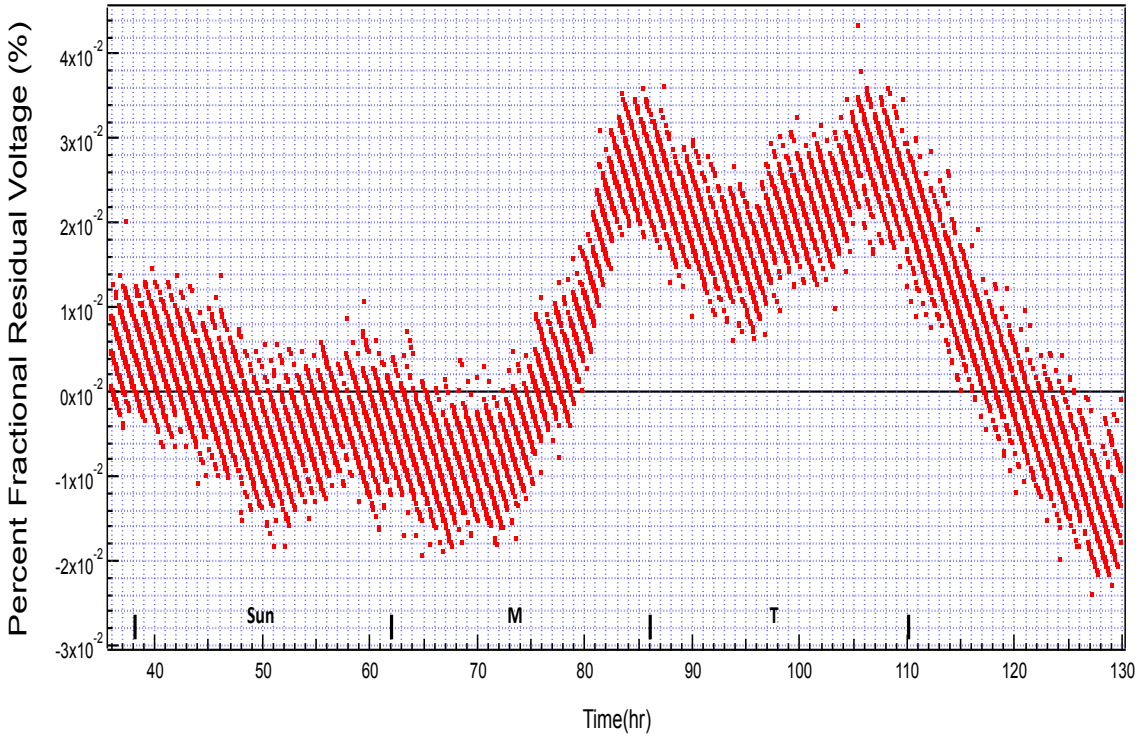

FIG 58. Percent fractional residual linear fit radiated PI applied voltage versus time: linear-linear plot.

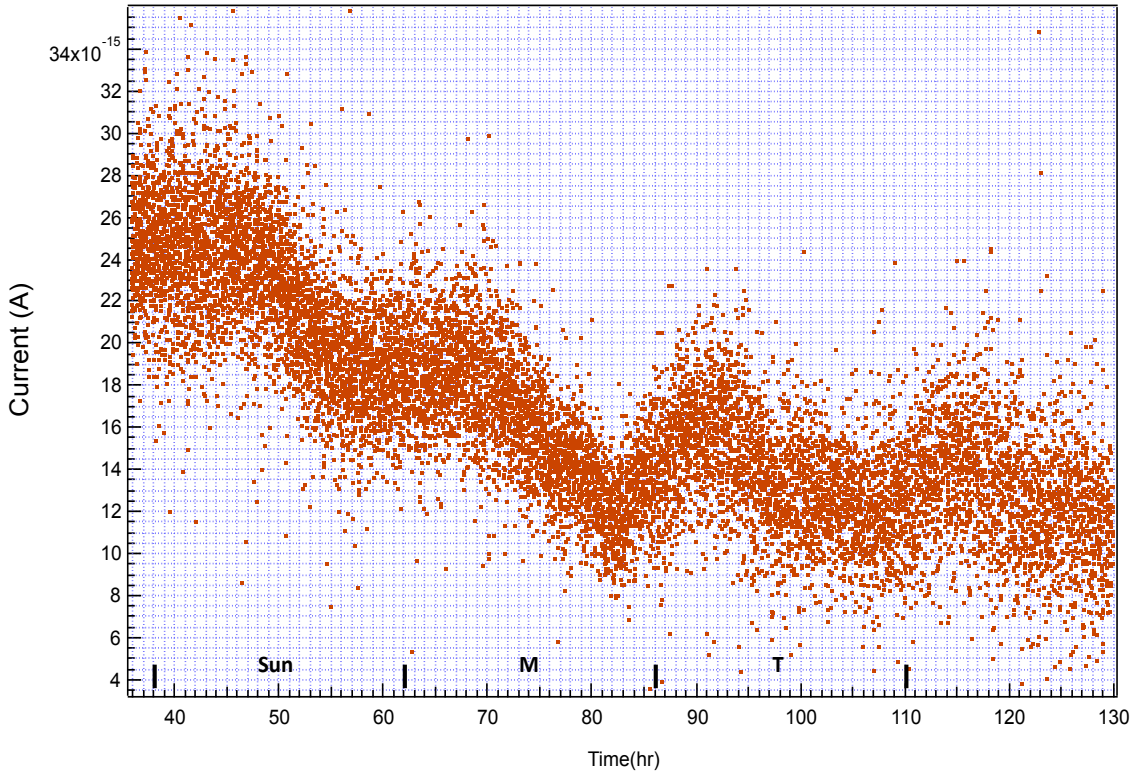

FIG 59. Radiated PI current versus time.

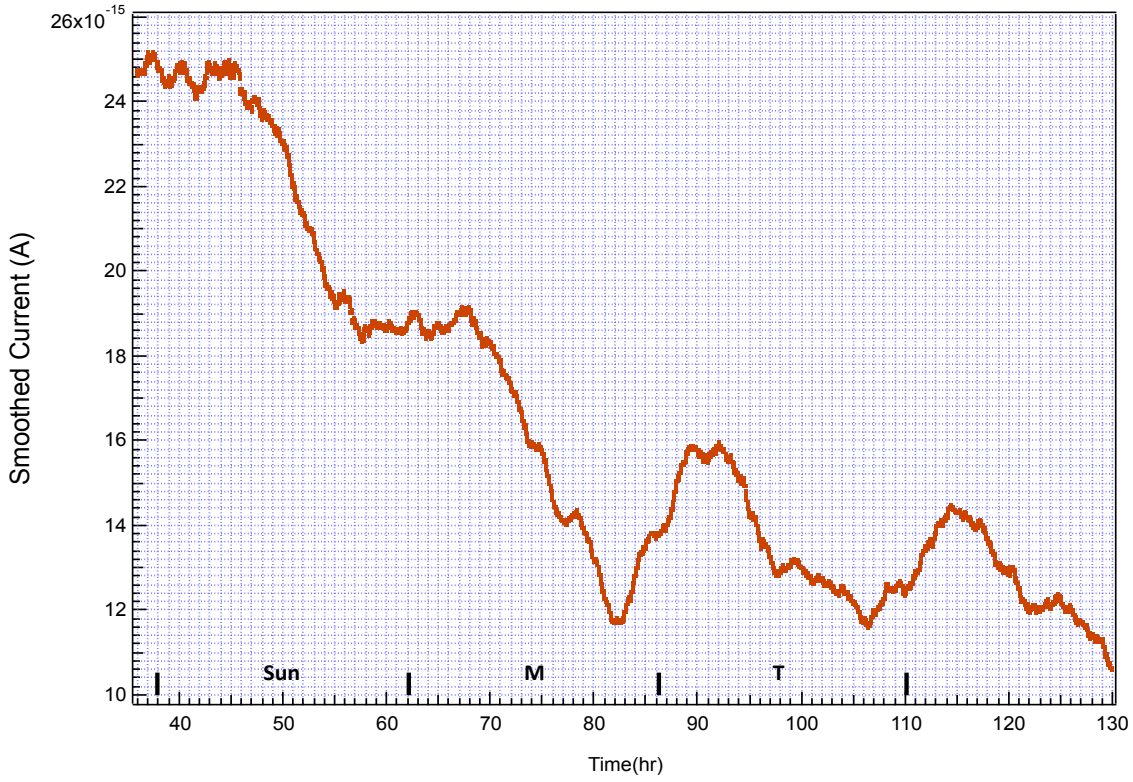

FIG 60. Smoothed radiated PI current versus time.

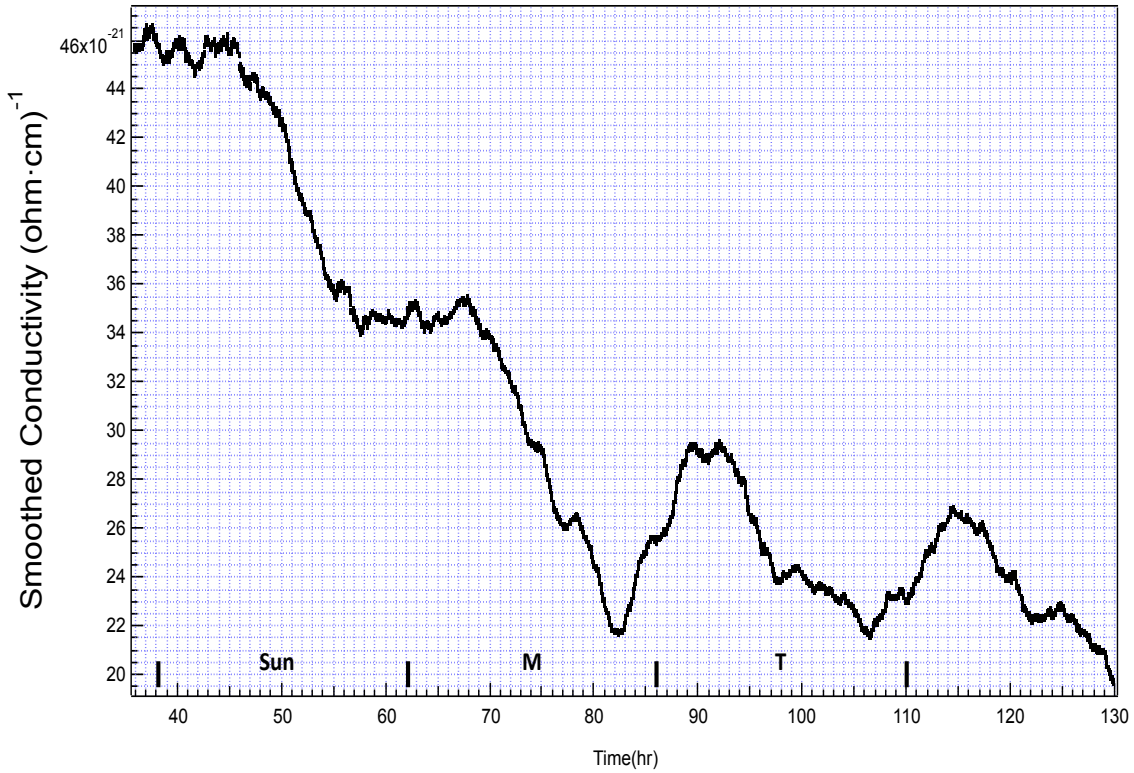

FIG 61. Smoothed radiated PI conductivity versus time: linear-linear plot.

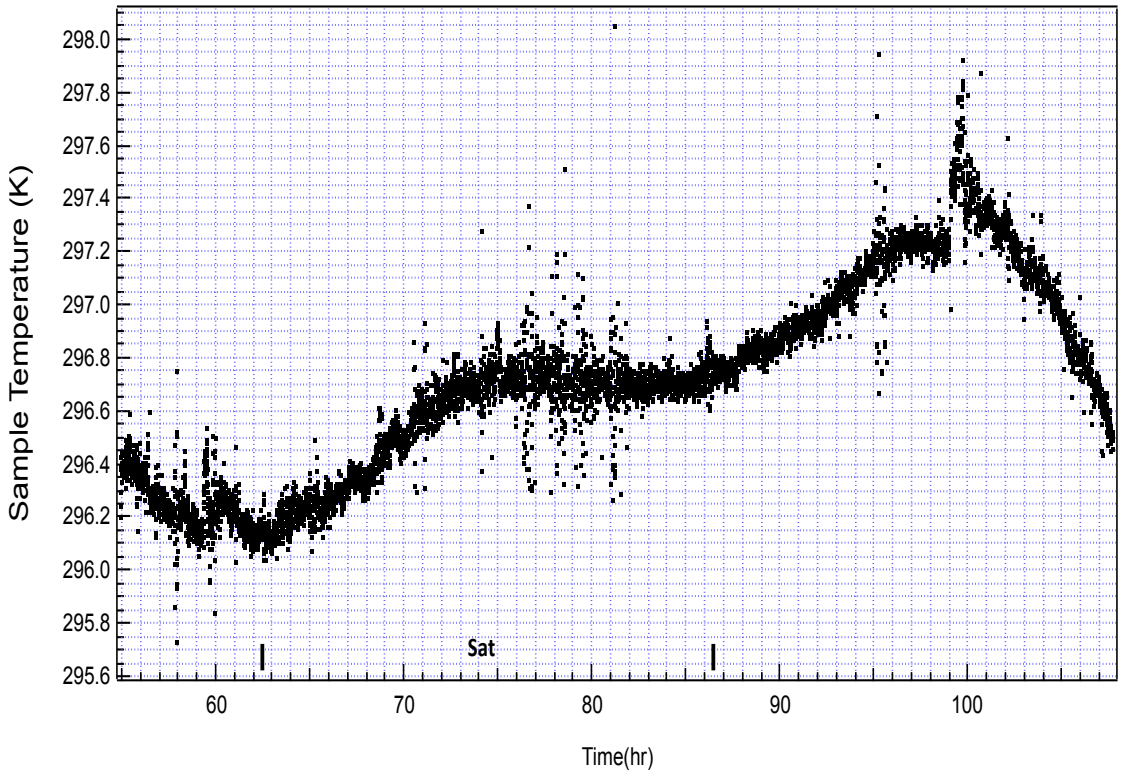

FIG 62. LDPE sample temperature versus time.

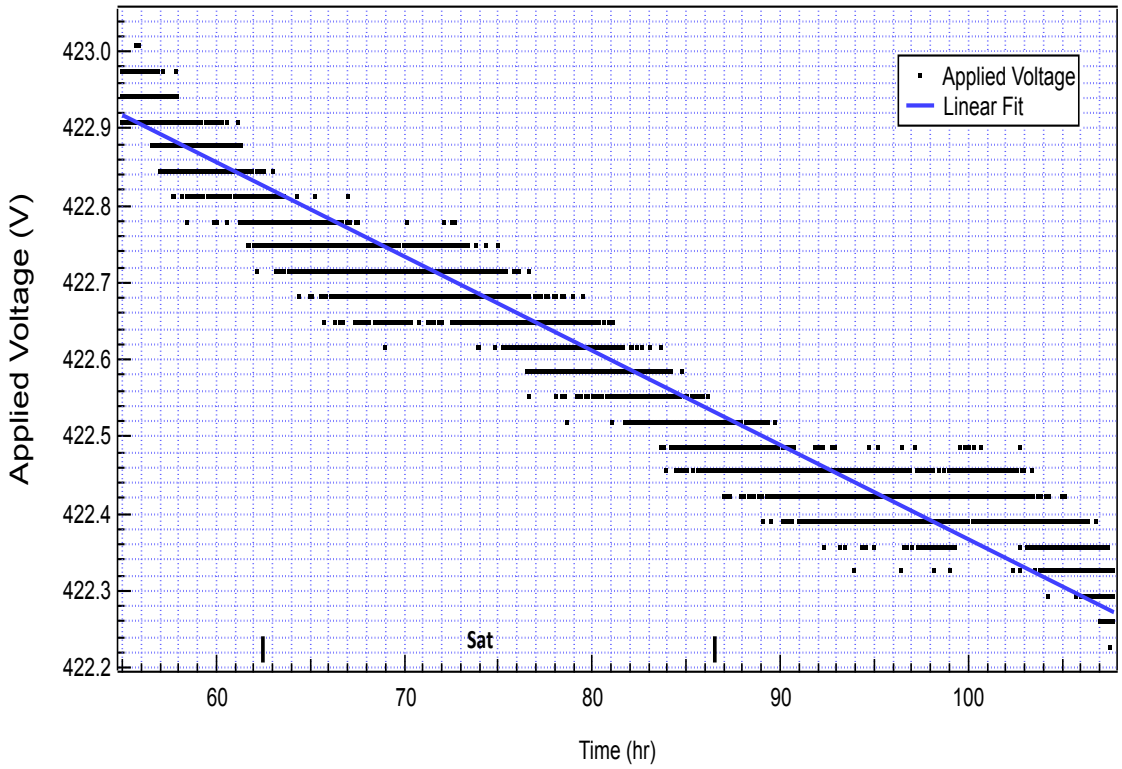

FIG 63. LDPE applied voltage versus time.

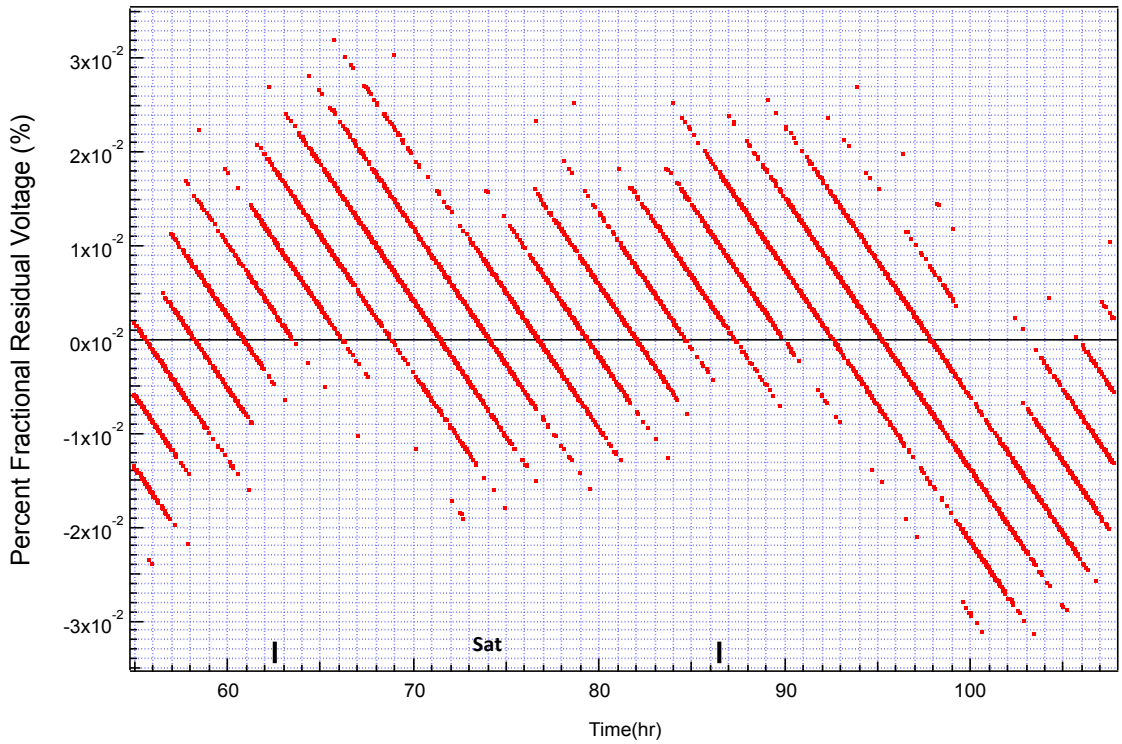

FIG 64. Percent fractional residual linear fit LDPE applied voltage versus time: linear-linear plot.

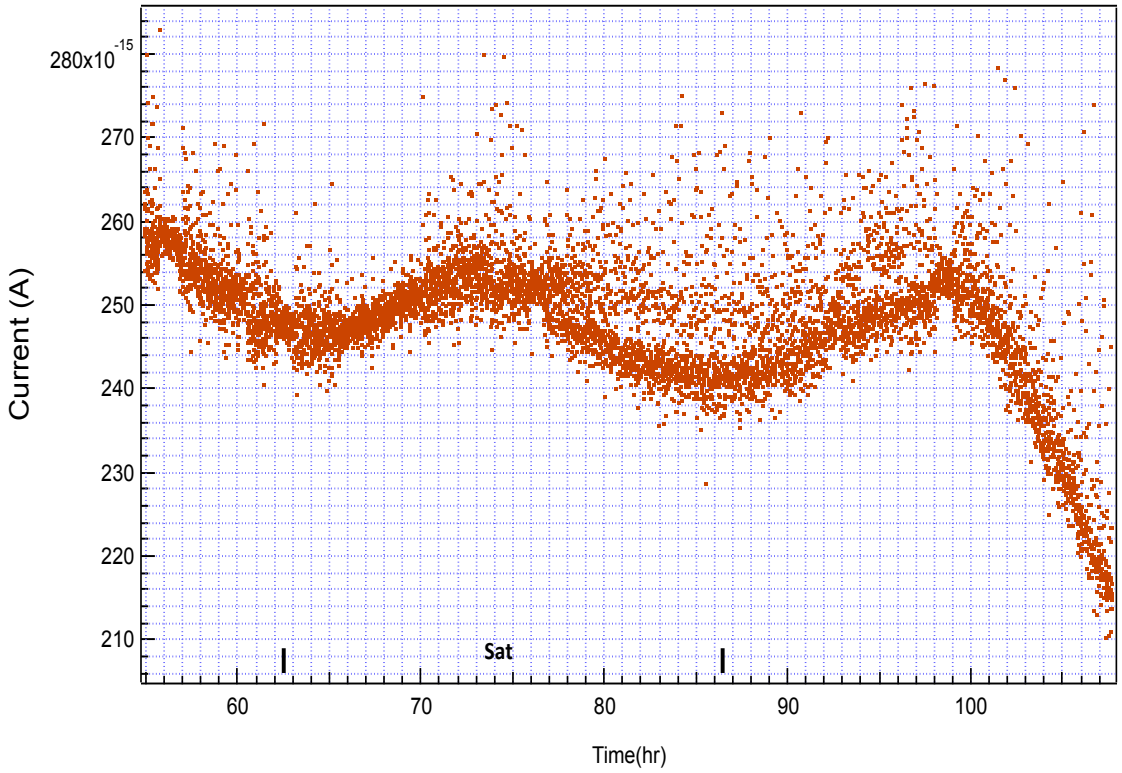

FIG 65. LDPE current versus time.

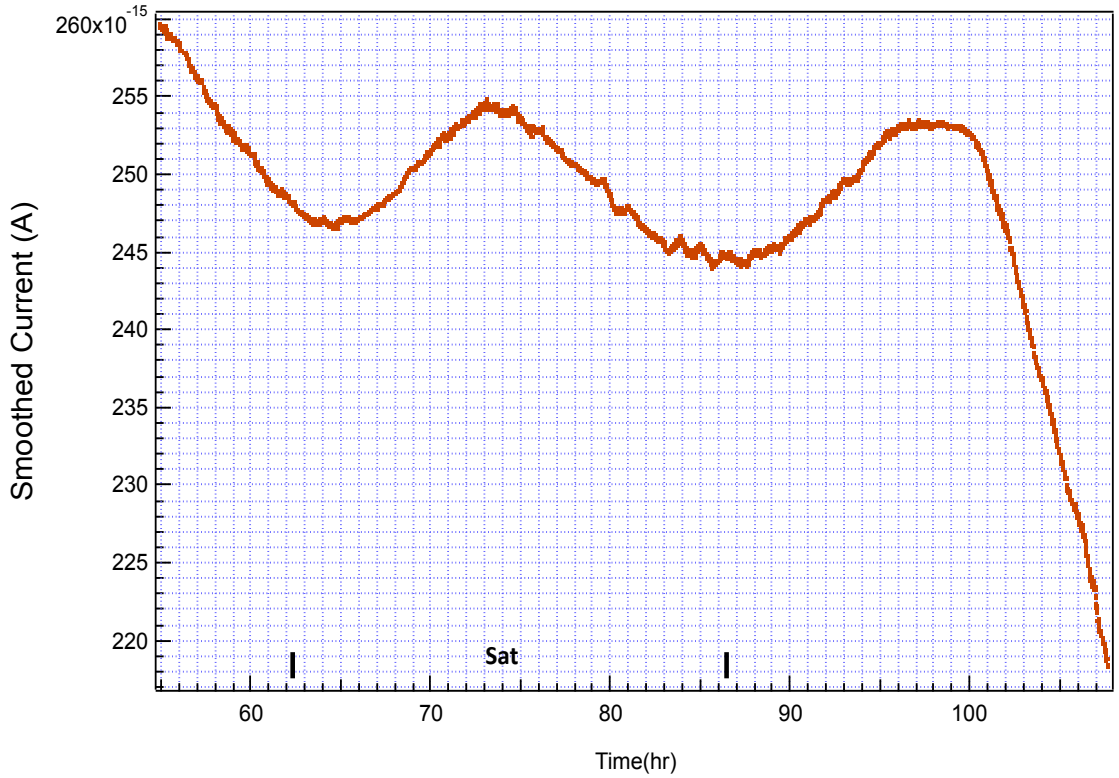

FIG 66. Smoothed LDPE current versus time.

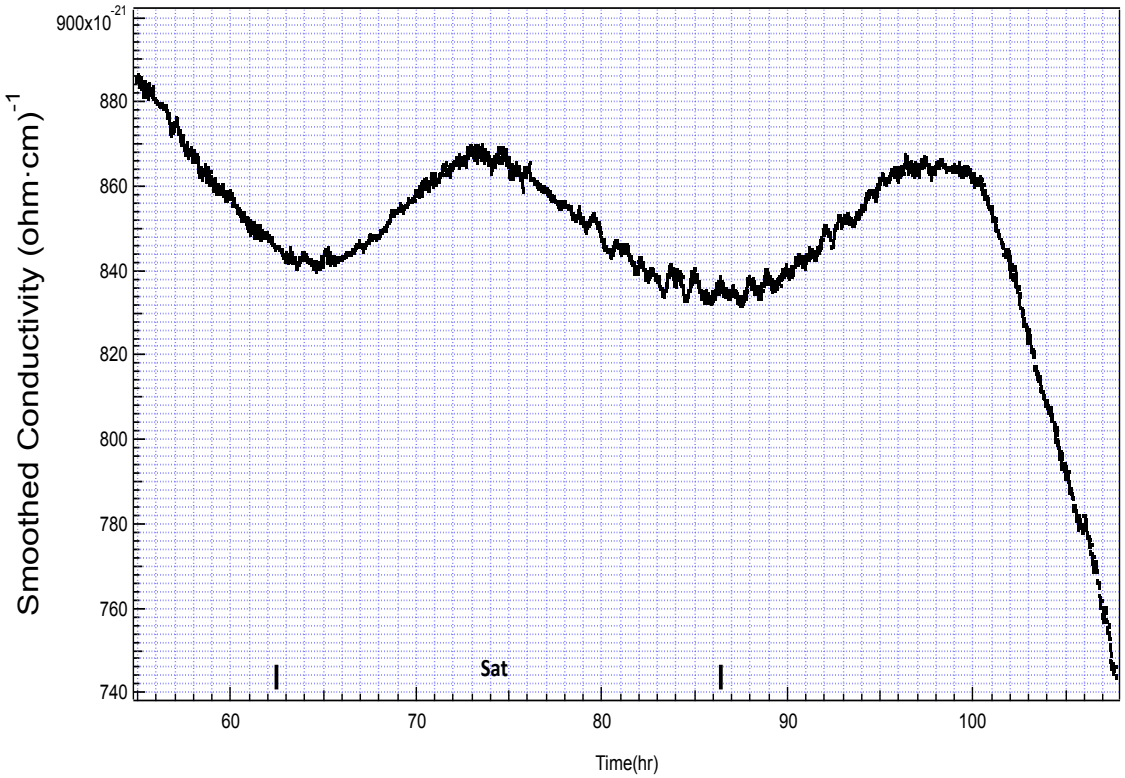

FIG 67. Smoothed LDPE conductivity versus time: linear-linear plot.

Table 3. Temperature fluctuation effects on conductivity.

Material	Average change in T per day (K)	Average % change in T per day	Average % change in σ per day	Average % change in σ per ΔT=1K
LDPE	0.9±0.2	0.29±0.07	9±7	10±6
Unirradiated PI	1.8±0.3	0.6±0.1	20±5	11±3
Radiated PI	0.5±0.2	0.17±0.07	37±8	80±20

The current data for unirradiated PI, radiated PI, and LDPE were smoothed, using the same box algorithm as was used in smoothing the conductivity data to produce Figures 54, 60, and 66. Figure 54 was smoothed using 200 points and is for unirradiated PI. Figure 60 was smoothed using 200 points as well and is for radiated PI. Lastly, Figure 66 was smoothed using 100 data points and is for LDPE. Figures 50, 56, and 62 show the sample temperatures during the time concerned for unirradiated PI, radiated PI, and LDPE, respectively.

Figures 51, 57, and 63, which show the applied voltage with the fit linear voltage drift for unirradiated PI (Figure 51), radiated PI (Figure 57), and LDPE (Figure 63), appear to show small changes in the voltage due to changes in temperature. The visible changes in voltage due to temperature are assumed to be the deviation in the voltage from the linear drift, which was due to battery discharge (compare Figures 50 and 51 for unirradiated PI, Figures 56 and 57 for radiated PI, and Figures 62 and 63 for LDPE). Figures 52, 58, and 64 show the percent fractional

residual voltage (calculated using a generalization of (3)) to more clearly show the deviation from linear voltage drift (Figure 52 for unirradiated PI, Figure 58 for radiated PI, and Figure 64 for LDPE). The displacement current due to these temperature fluctuations with time was calculated using the following equation

$$I_D = \frac{\varepsilon_0 A}{d}\frac{\partial V}{\partial t} \tag{6}$$

where I_D is the displacement current, A is the area of the electrode, d is the distance between the plates (here, the sample thickness), and $\frac{\partial V}{\partial t}$ is the derivative of the applied voltage with respect to time. First, the linear voltage drift was subtracted from the applied voltage data. Then, the maximum value of $\frac{\partial V}{\partial t}$ was calculated from the resulting graph. From this, the maximum value for I_D was calculated for unirradiated PI, radiated PI, and LDPE was calculated. The maximum values for $\frac{\partial V}{\partial t}$ were as follows: 20.1 mV/hr for unirradiated PI, 30.6 mV/hr for radiated PI, and 12.1 mV/hr for LDPE. This resulted in the following maximum values for displacement current: $3.31\text{x}10^{-16}$ A for unirradiated PI, $5.05\text{x}10^{-16}$ A for radiated PI, and $2.00\text{x}10^{-16}$ A for LDPE. Comparing these values of displacement current to the actual fluctuations in current shown in Figures 54, 60, and 66 show that these displacement currents could in no way account for the changes in current shown in the data. However, Figures 53, 59, and 65 show that the current fluctuates on almost the same 24 hr temporal cycles as the changes in temperature (Figures 50, 56, and 62). The smoothed current graphs show that the fluctuations in current are synchronized with fluctuations in temperature (Figure 50 for unirradiated PI, Figure 56 for radiated PI, and Figure 62 for LDPE). Furthermore, the smoothed current graphs show exactly the same fluctuations as are shown in the smoothed conductivity; the main difference between the conductivity and current graphs seems to be a scaling factor (compare Figures 54 and 55 for unirradiated PI, Figures 60 and 61 for radiated PI, and Figures 66 and 67 for LDPE).

Thus, the fluctuations in conductivity that seem to fluctuate with temperature are due mainly to fluctuations in current caused by changes in temperature. These changes in conductivity due to the temperature changes are different for unirradiated PI, radiated PI, and LDPE, as shown in Table 3. The change in conductivity for a 1K change in temperature for unirradiated PI and LDPE are the same within error, but the change in radiated PI is approximately eight times greater. This would indicate that the changes in conductivity, from the changes in current, are due to the fluctuations in temperature affecting the material and not the instrumentation.

Assuming that the conductivity is proportional to a simple Boltzmann distribution,

$$\sigma \propto e^{-\Delta E/k_B T} \tag{7}$$

and assuming that the trap states affected by this temperature range can be approximated as one state (E_U for unirradiated PI (σ_U) and E_R for radiated PI (σ_R)), the change in energy states due to irradiation may be approximated as follows:

$$\frac{\sigma_R}{\sigma_U} = \frac{80}{11} = e^{-\Delta E_R / k_B T} \Big/ e^{-\Delta E_U / k_B T} = e^{-[\Delta E_R - \Delta E_U] / k_B T} \quad (8)$$

The averaged temperature for the radiated and unirradiated PI samples, during the period when the samples had reached equilibrium, was 297.7 K. So, assuming this single temperature for both unirradiated and radiated PI, the calculation continues as follows:

$$\ln\frac{80}{11} * k_B T = (\Delta E_U - \Delta E_R) \cong 51 meV \quad (9)$$

Because PI is orange, its band gap energy can be calculated to be approximately 2 eV assuming frequencies of 480-520 THz for orange light. Therefore, using the above assumptions, the change effected by radiating PI was approximately a 51meV, or 2-3% of the band gap energy, shift in the energy level in PI that is activated at around room temperature.

The calculated values for α also lend credence to (2). According to the model of conductivity in (2), α_{disp} should equal α_{trans}. This is true within acceptable error for the unirradiated PI, radiated PI, and LDPE data shown (Table 2). Additionally, (1 – α) + (1 + α) =2 is true for PI, radiated PI, and LDPE to within error which is predicted by [1]. Both of these factors support the model and theory of conductivity in [1], which is shown in (2).

According to [7], the conductivity of unirradiated PI was measured, using the charge storage conductivity (CSC) method, to be >5x10^{19} Ω·cm. The dark conductivity of unirradiated PI measured in this project corresponds to a resistivity of (7.4±0.1)x10^{19} Ω·cm (±2%) and ±11% systematic uncertainty. Therefore, this project's result is entirely in agreement with [7] and is accurate to 0.1x10^{19} Ω·cm. This means that the CVC method can achieve the same results as the CSC method with greater accuracy. Which leads to another conclusion of this project, that a primary factor in obtaining highly accurate data is the time allowed for data collection. Long time scales, far longer than anticipated at the start of the project, are required to measure the conductivity accurately and capture the different conductivity mechanisms. Initial data collection times were on the order of 20 hrs. Later, long data collection times (100-230 hr) were attempted and it was determined that charge fronts can take from 25 to 40 hours to travel the approximately 25 μm width of the sample as measured by the transit time crossover from dispersive to transit conductivity.

It is interesting to note that, while the dark conductivity of unirradiated PI and radiated PI are not different by even one order of magnitude, they differ by 15 hr in their transit times (Table 2). It is hypothesized this may be due to radiation increasing the number of shallow energy defects in the radiated PI. This could allow for a decreased transit time and would be consistent with a similar increase in

temperature dependence of conductivity in PI after radiation, which is what was observed in this experiment with radiated PI.

In comparing the USU CVC chamber to commercial systems, the best commercial system, by Keithley, can measure resistivities as high as $1x10^{18}$ Ω·cm according to instrumentation specifications and, under ideal circumstances, is capable of measuring resistivities of up to approximately $1x10^{19}$ Ω·cm. In this project, the CVC chamber measured up to $(7.4\pm0.1)x10^{19}$ Ω·cm and, at 780 V, presently has a theoretical limit of $5x10^{21}$ Ω·cm. Thus, the USU CVC system, in its present configuration, is 500 to 5000 times more sensitive than standard commercial systems.

Future work with the CVC chamber includes improving the conductivity model of (2), continuing to measure the conductivity of radiated samples, and measuring the temperature dependence of material conductivity. To improve the conductivity model in (2), it is recommended that a more complex description of polarization be developed. As shown in Figures 16 and 31, including more polarization terms increases the physical accuracy of the model for unirradiated PI and radiated PI, resulting in (4). However, merely adding extra exponentials to different parts of the data may not be the best method of developing (2) further. The improved polarization contribution should have terms that correspond to the actual physical polarization processes taking place. To test this, the CVC chamber data collection software will likely need to be modified to take an increased number of data points in the first few seconds and minutes after the voltage is applied. An additional term will also need to be included in the model to account for the finite rise time of the voltage source [1].

Some preliminary testing of the temperature dependence of LDPE and PI conductivity was attempted and some analysis of temperature dependence was shown in this paper. However, in-depth analysis and data collection of temperature dependence was abandoned in favor of taking room temperature data to study and fit that with the model from [1]. The CVC chamber is currently equipped with both heating elements and a cooling system. So, studying temperature dependence will not require excessive chamber modification.

References

[1] J. Dekany, A.M. Sim, J. Brunson, and J.R. Dennison, IEEE Trans. on Plasma Sci. **41**, 3565 (2013).
[2] J. Dekany, senior thesis, Utah State University, 2010.
[3] R. Zallen, The Physics of Amorphous Solids (John Wiley & Sons, New York, 2008), p. 276 and 284.
[4] A. Sim, Ph.D. thesis, Utah State University, 2013.
[5] P. Lundgreen, senior thesis, 2014.
[6] J. Brunson, Ph.D. thesis, 2010.
[7] P. Swaminathan, J.R. Dennison, A.M. Sim, J. Brunson, E. Crapo, and A.R. Frederickson. "Comparison of classical and charge storage methods for determining conductivity of thin film insulators." (2004).
[8] J.R. Dennison and J. Brunson, IEEE Trans. on Plasma Sci. **36**, 2246 (2008).